This is a repository copy of *Stick-slip like behavior in shear fracture propagation including the effect of fluid flow*.

RESEARCH ARTICLE

Stick-slip like behavior in shear fracture propagation including the effect of fluid flow

Tim Hageman 🆔 | René de Borst 🆔

Department of Civil and Structural Engineering, University of Sheffield, Sheffield, UK

Correspondence
René de Borst, Department of Civil and Structural Engineering, University of Sheffield, Sheffield S1 3JD, UK.
Email: r.deborst@sheffield.ac.uk

Funding information
This work is supported by Horizon 2020 European Research Council Grant 664734 "PoroFrac."

Abstract

Shear-based fracture propagation in fluid-saturated porous materials is investigated using a displacement–pressure formulation that includes acceleration and inertial effects of the fluid. Pressure-dependent plasticity with a nonassociated flow rule is adopted to realistically represent the stresses in the porous bulk material. The domain is discretized using unequal order T-splines and cast into a finite element method using Bézier extraction. An implicit scheme is used for the temporal integration. The solid acceleration-driven fluid flow reacts to stress waves, but it results in pressure oscillations. Adding fluid acceleration terms dampens these oscillations and increases the fluid pressure near the fracture tips. By simulating a typical shear fracture case, it is shown that stick-slip like, or stepwise, fracture propagation occurs for a high permeability, also upon mesh refinement. The acceleration driven fluid flow results in a build-up of pressure near the fracture tip. Once this pressure region encompasses the fracture tip, propagation arrests until the pressure has diffused away from the crack tip, after which propagation is resumed and the build-up of pressure begins anew. This results in a stick-slip like behavior, with large arrests in the fracture propagation. Stepwise propagation related to the initial conditions has also been observed, but disappears once the fracture length exceeds the size of the region influenced by the initial conditions.

KEYWORDS
Cosserat continuum, isogeometric analysis, porous medium, shear fracture, stepwise fracture propagation

1 | INTRODUCTION

Seismic activity, either involving preexisting faults or new fractures, is related to changes in the interstitial fluid pressure in the surrounding porous rock.[1–4] Observations and laboratory experiments have shown that the presence of fluids can induce instabilities[5] and that increases in the fluid pressure can trigger earthquakes.[6] Simulations have further shown that changes in the fluid pressure can result in shear fracture propagation,[7,8] but also in arresting already propagating fractures.[9]

Simulations on shear-based fracture propagation are typically combined with off-fault plasticity with a nonassociated flow rule, either assuming drained or undrained behavior for the porous bulk material.[10–13] These simulations show that inclusion of the fluid has a large impact on the plastic strains. However, using a "drained" assumption neglects the pressure changes due to compression and the inertial effects of the fluid required to distribute local pressure increases. While the undrained assumption gives a better representation in the low-permeability limit, it neglects fluid diffusion. Indeed, allowing fluid diffusion has been shown to alter the plastic strains significantly,[14] and simulations without plasticity have shown the influence of the fluid diffusion on the fracture propagation.[15] Simulations without plasticity and acceleration-driven flow have shown that the interstitial fluid pressure can potentially stop the fracture from propagating.[16]

The acceleration of the fluid is often neglected in the expression for the fluid velocity in Darcy's law.[17–19] This is a reasonable assumption for low-frequency responses, but it is less clear whether this assumption holds close to a propagating fracture considering the accelerations that occur around the crack tip. Simulations have shown that the presence of these accelerations invalidates the assumption of a low-frequency response and that neglecting the fluid acceleration terms results in different solutions.[20] Additionally, the fluid acceleration term in Darcy's law damps the pressure and stress waves,[21–23] and therefore, results in different values for the stresses near the fracture tip, which has been shown using a simplified formulation.[24] Also when simulating porous materials with a relatively high porosity and permeability, neglecting this term causes differences in the solution.[25]

Recently, several authors have argued that the propagation of fractures in porous materials is not smooth, but stepwise.[26–29] This stepwise propagation is observed in experiments with pressurized fractures,[30–33] resulting in pressure oscillations at the inlet. Stepwise fracture propagation has also been argued to be one of the sources of intermittent earthquakes.[34] Results from simulations, however, rarely show a stepwise propagation. It was observed to depend on the element size,[35,36] but disappeared upon mesh refinement,[37–39] and therefore, was concluded not to have a physical origin.

Simulations exhibiting stepwise fracture propagation were, however, published in Refs. 40, 41, but the numerical scheme employed may have promoted this phenomenon. Stepwise propagation of pressurized fractures that are independent of the element size has also been shown using a hybrid peridynamics/finite element approach,[42] resulting in pressure oscillations at the inlet similar to those observed experimentally.

Most of this research was aimed at pressurized fractures, while stepwise fracture propagation in shear has also been observed experimentally. Stepwise propagation was observed by Ref. 43 when using coarse meshes, but this disappeared upon mesh refinement, even though it was claimed to have a physical origin.[29] Therefore, we believe that so far there are no conclusive simulations that reveal the existence of a stepwise shear fracture propagation, and under which conditions and for which physical parameter values, they occur.

Our aim is to investigate stepwise shear fracture propagation observed in fluid-saturated porous materials. For this purpose, we will first derive the governing equations, neglecting as few terms as possible, while adhering to the standard displacement–pressure formulation. Nonassociated plasticity is included in this scheme to accurately represent reality, and a Cosserat continuum is used to resolve mesh sensitivity and convergence issues that can originate from the use of nonassociated plasticity. The result is a monolithic scheme that includes nonassociated plasticity, shear-based fracture propagation, and acceleration-driven fluid flows.

After deriving the governing equations and describing the method used to include all acceleration terms in Section 2, we will show the effects of including these acceleration terms in Section 4, informing the decisions made for which terms are included in the remaining analysis. Through a mesh refinement study and simulations with varying permeability, we will analyze several types of stepwise fracture propagation in Sections 5. Finally, a second case is simulated in Section 6, showing that the occurrence of stepwise propagation of shear fractures is case dependent.

2 | GOVERNING EQUATIONS

The porous material is modeled as a Cosserat continuum, describing the kinematics of the (two-dimensional) solid by the displacements u_x and u_y and a Cosserat microrotation ω_z.[44,45] A Cosserat continuum introduces an internal length scale ℓ_c. It removes the ill-posedness and the ensuing the mesh dependence caused by the nonassociated plasticity,[46–49] and maintains the quadratic convergence of Newton–Raphson schemes used to solve nonlinear boundary value problems.[50]

2.1 | Including fluid inertia terms

The porous medium is described using the total momentum balance of the solid and fluid, the mass balance for the fluid, and the momentum balance for the fluid combined with Darcy's law.[18,19] These equations can be written in a form that

incorporates a Cosserat continuum as:

$$\boldsymbol{L}^T(\boldsymbol{\sigma}_s - \alpha p\boldsymbol{m}) - \boldsymbol{\rho}_s(1 - n_f)\ddot{\boldsymbol{u}}_s - \boldsymbol{\rho}_f n_f \boldsymbol{I}_c^T \ddot{\boldsymbol{u}}_f - \boldsymbol{\rho}_f \boldsymbol{I}_c^T(\boldsymbol{q} \cdot \boldsymbol{\nabla})\boldsymbol{q} = \boldsymbol{0}, \tag{1}$$

$$\frac{1}{M}\dot{p} + \alpha\boldsymbol{\nabla} \cdot (\boldsymbol{I}_c\dot{\boldsymbol{u}}_s) + \boldsymbol{\nabla} \cdot \boldsymbol{q} = 0, \tag{2}$$

$$\boldsymbol{q} = n_f(\dot{\boldsymbol{u}}_f - \boldsymbol{I}_c\dot{\boldsymbol{u}}_s) = -\frac{k}{\mu}\left(\boldsymbol{\nabla}p + \rho_f\ddot{\boldsymbol{u}}_f + \frac{\rho_f}{n_f}(\boldsymbol{q} \cdot \boldsymbol{\nabla})\boldsymbol{q}\right), \tag{3}$$

using the Biot modulus M, the Biot coefficient α, the intrinsic permeability k, the fluid viscosity μ, the porosity n_f, and the interstitial fluid pressure p (with compression taken as positive). The displacement of the solid material is described by $\boldsymbol{u}_s^T = [u_x\ u_y\ \omega_z]_s$ and $\boldsymbol{u}_f^T = [u_x\ u_y]_f$ describes the displacements of the fluid. Next to the standard Cauchy stress components, the solid stress vector $\boldsymbol{\sigma}_s$ includes the couple stress introduced by the Cosserat continuum, $\boldsymbol{\sigma}_s^T = [\sigma_{xx}, \sigma_{yy}, \sigma_{zz}, \sigma_{xy}, \sigma_{yx}, m_{xz}/\ell_c, m_{yz}/\ell_c]$. The Darcy fluid flux describes the velocity of the fluid relative to the solid, $\boldsymbol{q}^T = [q_x\ q_y]$, using the matrix $\boldsymbol{I}_c$ to only select the displacements, and to eliminate the Cosserat micro-rotation. The matrices used in Equations (1)–(3) are for a two-dimensional domain given by:

$$\boldsymbol{L}^T = \begin{bmatrix} \frac{\partial}{\partial x} & 0 & 0 & 0 & \frac{\partial}{\partial y} & 0 & 0 \\ 0 & \frac{\partial}{\partial y} & 0 & \frac{\partial}{\partial x} & 0 & 0 & 0 \\ 0 & 0 & 0 & -1 & 1 & \ell_c\frac{\partial}{\partial x} & \ell_c\frac{\partial}{\partial y} \end{bmatrix} \qquad \boldsymbol{m} = [1\ 1\ 1\ 0\ 0\ 0\ 0]^T \qquad \boldsymbol{\rho}_s = \begin{bmatrix} \rho_s & 0 & 0 \\ 0 & \rho_s & 0 \\ 0 & 0 & \Theta \end{bmatrix} \qquad \boldsymbol{\rho}_f = \begin{bmatrix} \rho_f & 0 & 0 \\ 0 & \rho_f & 0 \\ 0 & 0 & 0 \end{bmatrix} \qquad \boldsymbol{I}_c = \begin{bmatrix} 1 & 0 & 0 \\ 0 & 1 & 0 \end{bmatrix}$$

with ρ_s and ρ_f the density of the solid and the fluid, respectively, and $\Theta = 2\rho_s\ell_c^2/(1 + \nu)$ the rotational inertia.[48]

The terms related to the convective momentum transport in Equations (1) and (3), $(\boldsymbol{q} \cdot \boldsymbol{\nabla})\boldsymbol{q}$, require separate degrees of freedom to be used for the fluid flux in order to obtain the gradients of the fluid flux. However, the effect of these terms is usually very small,[18] and these terms will therefore be neglected. This allows the interior of the porous material to be described using only the solid displacement $\boldsymbol{u}$ and the interstitial fluid pressure p (and history variables).

To eliminate the fluid acceleration term in Equation (1), the definition of the Darcy fluid flux is substituted for the fluid acceleration term, resulting in:

$$\boldsymbol{L}^T(\boldsymbol{\sigma}_s - \alpha p\boldsymbol{m}) - \bar{\boldsymbol{\rho}}\ddot{\boldsymbol{u}}_s - \boldsymbol{\rho}_f\boldsymbol{I}_c^T\dot{\boldsymbol{q}} = \boldsymbol{0} \tag{4}$$

with volume averaged density $\bar{\boldsymbol{\rho}} = (1 - n_f)\boldsymbol{\rho}_s + n_f\boldsymbol{\rho}_f$. The effect of including separate inertia terms, compared to the more commonly taken approach of assuming the fluid inertia term $\dot{\boldsymbol{q}}$ to be negligible,[18,42,51–53] will be investigated in Section 4.

The acceleration of the fluid at time $t + \Delta t$ is determined using a θ-scheme:

$$\dot{\boldsymbol{q}}^{t+\Delta t} = \frac{1}{\theta\Delta t}\left(\boldsymbol{q}^{t+\Delta t} - \boldsymbol{q}^t\right) + \left(1 - \frac{1}{\theta}\right)\dot{\boldsymbol{q}}^t. \tag{5}$$

Using this temporal discretization, the momentum balance of the fluid combined with Darcy's law, Equation (3), is rewritten in a partial time discretized form as:

$$\boldsymbol{q}^{t+\Delta t} = -\frac{k}{\mu}\left(\boldsymbol{\nabla}p^{t+\Delta t} + \rho_f\left(\boldsymbol{I}_c\ddot{\boldsymbol{u}}^{t+\Delta t} + \frac{1}{n_f}\dot{\boldsymbol{q}}^{t+\Delta t}\right)\right), \tag{6}$$

$$\boldsymbol{q}^{t+\Delta t} = -\frac{k}{\mu}\left(\boldsymbol{\nabla}p^{t+\Delta t} + \rho_f\left(\boldsymbol{I}_c\ddot{\boldsymbol{u}}^{t+\Delta t} + \frac{1}{n_f}\left(\frac{1}{\theta\Delta t}\left(\boldsymbol{q}^{t+\Delta t} - \boldsymbol{q}^t\right) + \left(1 - \frac{1}{\theta}\right)\dot{\boldsymbol{q}}^t\right)\right)\right). \tag{7}$$

Using the values at the old time step, $\boldsymbol{q}^t$ and $\dot{\boldsymbol{q}}^t$, as history variables results in an explicit expression for the fluid flux, only dependent on the displacement and pressure:

$$\boldsymbol{q}^{t+\Delta t} = \left(1 + \frac{\rho_f k}{n_f\mu\theta\Delta t}\right)^{-1}\left(-\frac{k}{\mu}\boldsymbol{\nabla}p^{t+\Delta t} - \frac{k\rho_f}{\mu}\boldsymbol{I}_c\ddot{\boldsymbol{u}}^{t+\Delta t} - \frac{k\rho_f}{\mu n_f}\left(\left(1 - \frac{1}{\theta}\right)\dot{\boldsymbol{q}}^t - \frac{1}{\theta\Delta t}\boldsymbol{q}^t\right)\right). \tag{8}$$

This expression is substituted in the mass conservation for the fluid, Equation (2), resulting in the partial time-discretized mass balance at time $t + \Delta t$:

$$\frac{1}{M}\dot{p}^{t+\Delta t} + \alpha\boldsymbol{\nabla}\cdot\left(\boldsymbol{I}_c\dot{\boldsymbol{u}}^{t+\Delta t}\right) + \left(1 + \frac{\rho_f k}{n_f\mu\theta\Delta t}\right)^{-1}\boldsymbol{\nabla}\cdot\left(-\frac{k}{\mu}\boldsymbol{\nabla}p^{t+\Delta t} - \frac{k\rho_f}{\mu}\boldsymbol{I}_c\ddot{\boldsymbol{u}}^{t+\Delta t} - \frac{k\rho_f}{\mu n_f}\left((1-\frac{1}{\theta})\dot{\boldsymbol{q}}^t - \frac{1}{\theta\Delta t}\boldsymbol{q}^t\right)\right) = 0. \quad (9)$$

Similarly for Equation (4), discretizing the time derivative of the fluid flux using Equation (5), and substituting the expression of the fluid flux at time $t + \Delta t$, Equation (8), results in:

$$\boldsymbol{L}^T\left(\boldsymbol{\sigma}_s^{t+\Delta t} - \alpha p^{t+\Delta t}\boldsymbol{m}\right) - \left(\bar{\boldsymbol{\rho}} - An_f\rho_f\right)\ddot{\boldsymbol{u}}_s^{t+\Delta t} + An_f\boldsymbol{I}_c^T\boldsymbol{\nabla}p^{t+\Delta t} + \rho_f\boldsymbol{I}_c^T(1-A)\left(\frac{1}{\theta\Delta t}\boldsymbol{q}^t - \left(1-\frac{1}{\theta}\right)\dot{\boldsymbol{q}}^t\right) = \boldsymbol{0} \quad (10)$$

with the constant A defined as:

$$A = \frac{\rho_f\frac{k}{\mu}}{n_f\theta\Delta t + \rho_f\frac{k}{\mu}}. \quad (11)$$

Simplifications are often made by assuming the porous medium to be either drained or undrained. In the drained limit, the pressure throughout the domain is equal to a reference pressure, and taken to be constant. This assumes that the interstitial fluid instantly attains a uniform pressure, and that the effects of the inertia related to the fluid fluxes required for this are negligible. In contrast, the undrained limit assumes no fluid flow, representing an impermeable porous material. Then, the only source of pressure changes is the compression of the solid and the interstitial fluid.

When the intrinsic permeability is low, the constant A and the fluid flux $\boldsymbol{q}^t$ both approach zero, and as a result, Equation (10) contains only a single inertia term. This is consistent with undrained formulations, in which the volume averaged density is used. All terms related to fluid fluxes also cancel from the mass balance, Equation (9), and $k = 0$ corresponding to the undrained formulation.

In contrast, when approaching the drained limit by using a large permeability, A becomes one. For this limit, the solid inertia term only depends on the density of the solid, with the fluid using a separate inertia term solely based on the pressure gradient. The effect of using a large permeability in the mass balance results in the acceleration-driven fluid flow becoming more significant. This can be observed from Equation (8). When a high permeability is used such that $(\rho_f k)/(n_f\mu\theta\Delta t) \gg 1$, the expression for the fluid flux becomes:

$$\boldsymbol{q}^{t+\Delta t} = -n_f\theta\Delta t\left(\frac{1}{\rho_f}\boldsymbol{\nabla}p^{t+\Delta t} + \boldsymbol{I}_c\ddot{\boldsymbol{u}}^{t+\Delta t} + \frac{1}{n_f}\left(\left(1-\frac{1}{\theta}\right)\dot{\boldsymbol{q}}^t - \frac{1}{\theta\Delta t}\boldsymbol{q}^t\right)\right).$$

This shows that the fluid flux is limited for higher permeabilities, and becomes independent of the intrinsic permeability and viscosity in this limit. This is in contrast with the drained assumption, where it is assumed that in the high-permeability limit, the fluid flux becomes large enough to limit any interstitial pressure changes. Therefore, differences between the drained assumption and the high-permeability cases are to be expected, with the cases with actively simulated fluid flow not approaching the drained limit. Instead, these high-permeability cases will approach the limit indicated by the above equation.

2.2 | Plasticity model

The stresses in the solid material are assumed to be linearly related to the elastic strain:

$$\boldsymbol{\sigma}_s^{t+\Delta t} = \boldsymbol{D}_e\left(\boldsymbol{\varepsilon}^{t+\Delta t} - \boldsymbol{\varepsilon}_p^{t+\Delta t}\right) \quad (12)$$

with $\boldsymbol{D}_e$ the linear-elastic stiffness matrix for a Cosserat continuum[49] and the total strain $\boldsymbol{\varepsilon}^{t+\Delta t} = \boldsymbol{L}\boldsymbol{u}^{t+\Delta t}$. A nonassociated Drucker–Prager plasticity model is used to model the plastic deformations, with the yield function and plastic potential

defined as:

$$f = \sqrt{3J_2} + \alpha_s p_s - k_s \qquad g = \sqrt{3J_2} + \beta_s p_s \tag{13}$$

with p_s the solid pressure (tension positive), J_2 the second invariant of the deviatoric stresses in a Cosserat continuum[45,54] and α_s, β_s, and k_s related to the angle of internal friction ϕ, dilatancy angle ψ, and cohesion c through:

$$\alpha_s = \frac{6\sin\phi}{3 - \sin\phi} \qquad \beta_s = \frac{6\sin\psi}{3 - \sin\psi} \qquad k_s = c\frac{6\cos\phi}{3 - \sin\phi}. \tag{14}$$

More implementation details related to the integration of the plastic strain and the used tangential stiffness matrix are given in Ref. 50.

2.3 | Discontinuity models

The discontinuity is modeled using interface elements, which are only present for the fracture. Ahead of this fracture, the material is considered fully intact and is governed by the equations for the poroelastic medium. It is assumed the fracture propagates in mode II, and is solely governed by the shear stress. Once the stresses in the continuum ahead of the fracture exceed the fracture criterion $|\sigma_{yx}| > -f_p \sigma_{yy}$,[55] the discontinuity is propagated and additional interface elements are inserted. This propagation criterion uses the peak coefficient f_p to model a cohesionless material, with the required shear stress for fracture propagation depending on the normal stress.

At the discontinuity, a discontinuous pressure model[39,56,57] has been used, which allows for a discontinuous pressure distribution across the fracture, with an independent pressure degree of freedom inside the fracture. For closed fractures, without fluid flow inside the fracture in the tangential direction, the mass balance inside the fracture is given by:

$$0 = \boldsymbol{n}_d^- \cdot \boldsymbol{q}^- + \boldsymbol{n}_d^+ \cdot \boldsymbol{q}^+ = k_i\left(p^+ + p^- - 2p_d\right), \tag{15}$$

and the fluid flux imposed on the porous material is given by:

$$\boldsymbol{n}_d^+ \cdot \boldsymbol{q}^+ = k_i\left(p^+ - p_d\right), \tag{16}$$

$$\boldsymbol{n}_d^- \cdot \boldsymbol{q}^- = k_i(p^- - p_d), \tag{17}$$

using the pressure inside the discontinuity p_d and the interstitial fluid pressures at the top and bottom walls of the fracture, p^+ and p^-, respectively. The normal vectors at the top and bottom of the fracture, $\boldsymbol{n}_d^+$ and $\boldsymbol{n}_d^-$, are taken as positive when pointing outward. The interface permeability k_i governs the amount of fluid that can flow across the fracture. It is an indication of the resistance to the fluid flow originating from plastic deformations and damage close to the discontinuity caused by the fracturing process. This interface permeability therefore allows to include the effects of damage and plasticity on the fluid flow, even though the region of these effects is smaller than the element size. To keep the formulation as simple as possible, the interface permeability will be assumed as constant.

In a local coordinate system, the tractions at the discontinuity are given by:

$$\tau_d^{\pm} = \begin{bmatrix} \tau_{ds} \\ \tau_{dn} - p_d \\ \tau_{\omega} \end{bmatrix}. \tag{18}$$

To prevent negative fracture opening heights, we set the following relations:

$$\tau_{dn} = d_n [\![u_n]\!] \qquad \tau_{\omega}/\ell^2 = d_{\omega} [\![\omega_z]\!] \tag{19}$$

with high values for the dummy stiffnesses d_n and d_{ω}, and $[\![u_n]\!]$ and $[\![\omega_z]\!]$ the jumps in the normal displacement and the microrotation, respectively. The tangential component of the interface traction is determined through an exponential

traction separation law:

$$\tau_t = f_r \tau_{dn} + (f_p - f_r) \, \tau_{dn} \exp(-2[\![dx]\!]/D_c) \tag{20}$$

with f_p and f_r the peak and residual coefficients of friction. D_c is the weakening distance, given by $D_c = 2\mathcal{G}_c/(f_p\tau_n - f_r\tau_n)$ where $\mathcal{G}_c$ is the fracture energy. The used exponential relation was preferred over the more commonly used linear degradation model[10,55,58] in order to retain a smooth function, which improves the convergence of the nonlinear solver. The maximum jump in the tangential displacement $[\![dx]\!]$ is treated as a history variable, and therefore, it is equal to the current tangential displacement jump $[\![u_t]\!]$, or constant when the current displacement is lower than the previously obtain tangential displacement.

2.4 | Discretization

The time discretization of Equations (9) and (10) has been carried out using a Newmark scheme for the displacements and a θ-scheme for the interstitial fluid pressure:

$$\dot{\boldsymbol{u}}^{t+\Delta t} = \frac{\gamma}{\beta \Delta t} \left(\boldsymbol{u}^{t+\Delta t} - \boldsymbol{u}_t \right) - \left(\frac{\gamma}{\beta} - 1 \right) \dot{\boldsymbol{u}}^t - \left(\frac{\Delta t \gamma}{2\beta} - \Delta t \right) \ddot{\boldsymbol{u}}^t, \tag{21}$$

$$\ddot{\boldsymbol{u}}^{t+\Delta t} = \frac{1}{\beta \Delta t^2} \left(\boldsymbol{u}^{t+\Delta t} - \boldsymbol{u}^t \right) - \frac{1}{\beta \Delta t} \dot{\boldsymbol{u}}^t - \left(\frac{1}{2\beta} - 1 \right) \ddot{\boldsymbol{u}}^t, \tag{22}$$

$$\dot{p}^{t+\Delta t} = \frac{1}{\theta \Delta t} \left(p^{t+\Delta t} - p^t \right) + \left(1 - \frac{1}{\theta} \right) \dot{p}^t. \tag{23}$$

This introduces history variables for the solid velocity and acceleration, and the fluid pressure change at time t. These history variables, and the old fluid flux $\boldsymbol{q}^t$ and fluid flux change $\dot{\boldsymbol{q}}^t$, are updated at the end of each time step. In contrast, the history variable for the plastic strain, $\boldsymbol{\varepsilon}_p^t$, and the interface displacement, $[\![dx]\!]$, are updated at the end of each time step and after each fracture propagation step. This ensures these path-dependent variables accurately capture the loading and unloading that can occur during fracture propagation.

The fracture propagation is considered to be part of the time step. Therefore, once a converged solution is achieved, the stresses ahead of the fracture tip are checked and if all these stresses exceed $f_t = -f_p \sigma_{yy}$, the fracture is propagated a single element (checked at both ends of the fracture). Afterwards, more iterations are carried out to again establish an equilibrium solution for the current time step and the new fracture length. Next, the propagation criterion is checked again. This is repeated until no further propagation occurs and a converged solution is reached, resulting in an implicit scheme for the governing equations and the fracture length.

T-splines have been used for the spatial discretization.[59,60] This allows a higher-order interelement continuity, resulting in continuous stresses and fluid fluxes between the elements.[61,62] Furthermore, by using T-splines, the displacement gradient, and thus the strains and stresses, can be directly evaluated at the boundaries of elements. This facilitates the fracture propagation criterion as it is not necessary to extrapolate stresses from the interior of the elements. The T-splines are used in a similar manner as traditional Lagrangian interpolants by using Bézier extraction, decomposing the spline-based functions in a linear combination of Bernstein polynomials.[63] This allows the displacement, the interstitial fluid pressure, and the pressure in the discontinuity to be expressed as a sum over all elements:

$$\boldsymbol{u} = \sum_{el=1}^{n_{el}} \boldsymbol{N}_s^{el} \boldsymbol{u}^{el}, \tag{24}$$

$$p = \sum_{el=1}^{n_{el}} \boldsymbol{N}_f^{el} \boldsymbol{p}^{el}, \tag{25}$$

$$p_d = \sum_{iel=1}^{n_{iel}} \boldsymbol{N}_{df}^{iel} p_d{}^{iel}, \tag{26}$$

with:

$$\boldsymbol{N}_s = \begin{bmatrix} \boldsymbol{N}_x & \boldsymbol{0} & \boldsymbol{0} \\ \boldsymbol{0} & \boldsymbol{N}_y & \boldsymbol{0} \\ \boldsymbol{0} & \boldsymbol{0} & \boldsymbol{N}_\omega \end{bmatrix}. \tag{27}$$

To fulfill the inf-sup condition,[64] and thus to prevent spurious oscillations, the interpolants for the solid displacement need to be an order higher than the interpolants for the fluid pressure. Therefore, quartic T-splines were used for the solid displacement, $\boldsymbol{N}_x$ and $\boldsymbol{N}_y$, whereas cubic T-splines were used for the interstitial and discontinuity fluid pressures, $\boldsymbol{N}_f$ and $\boldsymbol{N}_{df}$ (only defined at the discontinuity). The inf-sup condition does not impose any requirements on the order of the interpolants for the Cosserat rotation $\boldsymbol{N}_\omega$, and it was chosen to use cubic T-splines to reduce the resulting number of degrees of freedom. For the elements and geometry of the quartic and cubic meshes to match, the interelement continuity of the meshes needs to be the same. This is achieved by repeating the mesh lines of the quartic T-spline mesh, resulting in both meshes having a C^2 interelement continuity, thus allowing for continuous and smooth stresses and fluid fluxes.

The discontinuity is represented using spline-based interface elements.[65–68] By using T-splines, these interface elements can be inserted only for the fractured elements, in contrast to B-splines that require the interface elements to be inserted along a line passing through the complete domain. This removes the need for a formulation for nonfractured interface elements.[69] The displacements and Cosserat microrotation are discontinuous across the interface elements,[70] with the tractions at the interface determined by Equation (18). The interstitial fluid pressure is also discontinuous across the discontinuity, with an additional degree of freedom added at the discontinuity to represent the pressure inside the discontinuity. The fluid flux between the porous material and the interior of the discontinuity is governed by Equations (15)–(17).

Using the discretization from Equations (21)–(26), the momentum balance from Equation (10) is discretized as:

$$\boldsymbol{f}_{ext} - \boldsymbol{f}_{int} - \boldsymbol{f}_d = \boldsymbol{0} \tag{28}$$

with the external force vector defined in a standard manner as:

$$\boldsymbol{f}_{ext} = \int_{\Gamma_t} \boldsymbol{N}_s^T \bar{\boldsymbol{t}} + \boldsymbol{N}_s^T \boldsymbol{R}^T \boldsymbol{S} \boldsymbol{R} \boldsymbol{N}_s \left(\frac{\gamma}{\beta \Delta t} (\boldsymbol{u}^{t+\Delta t} - \boldsymbol{u}_t) - \left(\frac{\gamma}{\beta} - 1 \right) \dot{\boldsymbol{u}}^t - \left(\frac{\Delta t \gamma}{2\beta} - \Delta t \right) \ddot{\boldsymbol{u}}^t \right) d\Gamma, \tag{29}$$

where $\bar{\boldsymbol{t}}$ is the traction imposed on the boundary of the domain, and $\boldsymbol{S}$ is the damping matrix used for the absorbing boundary conditions:[50,71]

$$\boldsymbol{S} = \rho_s \begin{bmatrix} c_p & 0 & 0 \\ 0 & c_s & 0 \\ 0 & 0 & 0 \end{bmatrix}, $$

using the pressure and shear stress wave speeds c_p and c_s. The internal force vector is given by:

$$\boldsymbol{f}_{int} = \int_\Omega \boldsymbol{B}^T \boldsymbol{\sigma}_s^{t+\Delta t} - \alpha \boldsymbol{B}^T \boldsymbol{m} \boldsymbol{N}_f \boldsymbol{p}^{t+\Delta t} \, d\Omega + \int_\Omega \boldsymbol{N}_s^T (\bar{\rho} - A n_f \rho_f) \boldsymbol{N}_s \left(\frac{1}{\beta \Delta t^2} (\boldsymbol{u}^{t+\Delta t} - \boldsymbol{u}^t) - \frac{1}{\beta \Delta t} \dot{\boldsymbol{u}}^t - \left(\frac{1}{2\beta} - 1 \right) \ddot{\boldsymbol{u}}^t \right) d\Omega$$

$$- \int_\Omega A n_f \boldsymbol{N}_s^T \boldsymbol{I}_c^T \nabla \boldsymbol{N}_f \boldsymbol{p}^{t+\Delta t} + (1 - A) \boldsymbol{N}_s^T \rho_f \boldsymbol{I}_c^T \left(\frac{1}{\theta \Delta t} \boldsymbol{q}^t - \left(1 - \frac{1}{\theta} \right) \dot{\boldsymbol{q}}^t \right) d\Omega$$

$$\tag{30}$$

using $\boldsymbol{B} = \boldsymbol{L}\boldsymbol{N}_s$. Finally, the forces related to the discontinuity are obtained from:

$$\boldsymbol{f}_d = \int_{\Gamma_d} \boldsymbol{N}_s^T \boldsymbol{R}^T (\tau_d)_{t+\Delta t} \, \mathrm{d}\Gamma_d \tag{31}$$

with $\boldsymbol{R}$ the rotation matrix at the discontinuity.

Similarly, mass conservation, Equation (9) is discretized as:

$$\boldsymbol{q}_{ext} - \boldsymbol{q}_{int} - \boldsymbol{q}_d = \boldsymbol{0} \tag{32}$$

with the external fluxes defined as:

$$\boldsymbol{q}_{ext} = \Delta t \int_{\Gamma_q} \boldsymbol{N}_f^T \overline{q} \, \mathrm{d}\Gamma \tag{33}$$

and the internal flux vector as:

$$
\begin{aligned}
\boldsymbol{q}_{int} = & -\int_\Omega \frac{1}{M} \boldsymbol{N}_f^T \boldsymbol{N}_f \left(\frac{1}{\theta}(\boldsymbol{p}^{t+\Delta t} - \boldsymbol{p}^t) + \Delta t \left(1 - \frac{1}{\theta}\right)\dot{\boldsymbol{p}}^t \right) \mathrm{d}\Omega \\
& - \int_\Omega \alpha \boldsymbol{N}_f^T \boldsymbol{I}_c \boldsymbol{B} \left(\frac{\gamma}{\beta}(\boldsymbol{u}^{t+\Delta t} - \boldsymbol{u}_t) - \Delta t \left(\frac{\gamma}{\beta} - 1\right)\dot{\boldsymbol{u}}^t - \Delta t^2 \left(\frac{\gamma}{2\beta} - 1\right)\ddot{\boldsymbol{u}}^t \right) \mathrm{d}\Omega \\
& - \frac{k\Delta t}{\mu}\left(1 + \frac{\rho_f k}{n_f \mu \theta \Delta t}\right)^{-1} \int_\Omega (\boldsymbol{\nabla}\boldsymbol{N}_f)^T \boldsymbol{\nabla}\boldsymbol{N}_f \boldsymbol{p}^{t+\Delta t} + \frac{\rho_f}{n_f}(\boldsymbol{\nabla}\boldsymbol{N}_f)^T \left(\left(1 - \frac{1}{\theta}\right)\dot{\boldsymbol{q}}^t - \frac{1}{\theta\Delta t}\boldsymbol{q}^t\right) \\
& + \rho_f (\boldsymbol{\nabla}\boldsymbol{N}_f)^T \boldsymbol{I}_c \boldsymbol{N}_s \left(\frac{1}{\beta\Delta t^2}(\boldsymbol{u}^{t+\Delta t} - \boldsymbol{u}^t) - \frac{1}{\beta\Delta t}\dot{\boldsymbol{u}}^t - \left(\frac{1}{2\beta} - 1\right)\ddot{\boldsymbol{u}}^t \right) \mathrm{d}\Omega.
\end{aligned}
\tag{34}
$$

The fluxes due to the fluid flow normal to the fracture are given by:

$$\boldsymbol{q}_d = k_i \Delta t \int_{\Gamma_d} \boldsymbol{N}_f^T \left(\boldsymbol{N}_{df}\, \boldsymbol{p}_d^{t+\Delta t} - \boldsymbol{N}_f \boldsymbol{p}^{t+\Delta t} \right) \mathrm{d}\Gamma, \tag{35}$$

and the mass balance for the interior of the fracture, Equation (15), is discretized as:

$$k_i \Delta t \int_{\Gamma_d} \boldsymbol{N}_{df}^T \boldsymbol{N}_f \left(\boldsymbol{p}^{+\,t+\Delta t} + \boldsymbol{p}^{-\,t+\Delta t} \right) - 2\boldsymbol{N}_{df}^T \boldsymbol{N}_{df}\, \boldsymbol{p}_d^{t+\Delta t} \, \mathrm{d}\Gamma_d = \boldsymbol{0}. \tag{36}$$

Equations (28), (32), and (36) are solved in a monolithic manner using a Newton–Raphson scheme. The system matrices used for this scheme are given in Appendix A. A quadratic convergence rate was obtained using these system matrices.

3 | DESCRIPTION OF THE CASE STUDIED

The effect of including pressure- and acceleration-driven fluid flows is now demonstrated by simulating a typical case that features a propagating shear fracture.[10,11] A domain of 500 m × 250 m is considered with an initial horizontal fracture in the center of the domain with a length of 75 m, see Figure 1. Only horizontal fracture propagation is allowed.

At the boundaries of the domain, absorbing boundary conditions are imposed to reduce the reflection of pressure and shear waves. External tractions are applied at the boundaries, $t_{xx} = 8.55$ MPa, $t_{yy} = 10$ MPa, $t_{xy} = t_{yx} = 1.8$ MPa. The porous material is characterized by a Young's modulus $E = 10$ GPa, a Poisson ratio $\nu = 0.25$, a Cosserat shear modulus $G_c = 4$ GPa, a Cosserat length scale $\ell_c = 1$ cm, and density $\rho_s = 2500$ kg/m³. A water-like fluid is used, using $\mu = 1$ mPa · s and $\rho_f = 1000$ kg/m³. The bulk modulus of the solid is $K_s = 10$ GPa, the fluid bulk modulus $K_f = 2$ GPa, the Biot coefficient $\alpha = 1.0$, a porosity $n_f = 0.3$, and the interface permeability $k_i = 10^{-10}$ m/Pas. The peak friction coefficient was set $f_p = 0.45$, the residual coefficient of friction $f_r = 0.045$, and fracture energy $\mathcal{G}_c = 17.4$ kJ/m². A cohesion-
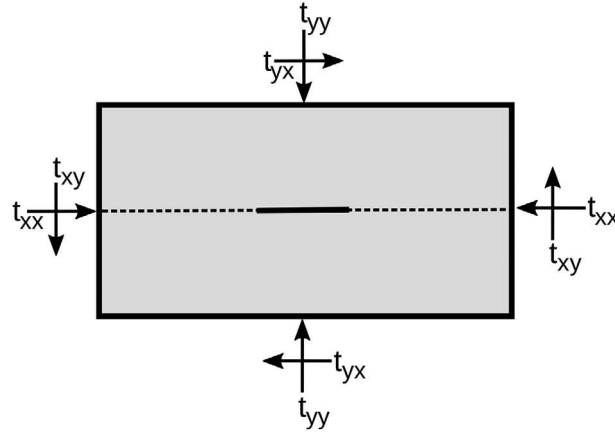
FIGURE 1 Geometry and applied traction of the simulated case

less, nondilatant Drucker–Prager plasticity model ($c = 0, \psi = 0°$) is adopted, with an angle of internal friction $\phi = 31°$. The intrinsic permeability of the porous material was varied between $k = 10^{-10}$ m^2 and $k = 10^{-7}$ m^2, and additional simulations were run using the undrained ($k = 0$ m^2) and the drained ($p = 0$ Pa and $q = 0$ m/s) assumptions. These values for the permeability cover the range from negligible effects of acceleration-driven flow to the fluid flux being dominated by inertial effects.

The spatial discretization uses cubic T-splines for the interstitial pressure, the discontinuity pressure, and the Cosserat microrotation, while quartic T-splines were used for the displacements. Three different meshes were used. The first mesh consists of a layer of 320×10 Bézier-extracted elements near the interface, surrounded by layers of 160×5 and 80×15 elements (hereafter referred to as 320×50). The second mesh adds an extra refinement layer of 640×10 elements at the interface, for a total of 60 elements in the vertical direction (referred to as 640×60). Finally, the third mesh halves all the elements, resulting in a mesh of 1280×120 elements.

The conditions at $t = t_0$ are a zero interstitial fluid pressure and a zero pressure at the discontinuity, with the solid being in equilibrium and without any plastic deformations at this time. This is imposed by simulating the first $t_0 = 1$ s of the simulation with time steps of $\Delta t = 0.01$ s with no plastic strains or fracture propagation being allowed, and a constant and zero pressure imposed in the domain. During this initial period, the discontinuity is not allowed to propagate and no plastic strains are allowed to occur (both the propagation criteria and the yield criteria are ignored). Furthermore, the interstitial pressure is constrained to $p = 0$ MPa in the complete domain. After this initial period, starting from $t = t_0$, the simulation is carried out using a time step $\Delta t = 0.04$ ms without the constraints that have been applied initially. The time step is such that even with the finest mesh, the fracture will only propagate over two elements (due to the symmetry) every 5–10 time steps. The temporal discretization for the solid displacement used $\beta = 0.4$ and $\gamma = 0.75$ as parameters, and for the temporal integration of the fluid $\theta = 1.0$.

4 | EFFECT OF THE FLUID INERTIA TERMS

The effect of terms that account for acceleration-driven fluid flow in the mass balance and separate inertia terms in the momentum balance is analyzed by adding these terms one-by-one. The first simulation uses only the pressure gradient-driven flow, the $\frac{k}{\mu}\nabla p$ term in Equation (6), and uses a single inertia term, thus neglecting the acceleration of the fluid relative to the porous material, $\dot{q} = 0$ in Equation (4). Next, the solid acceleration-driven flow is added, $\frac{k\rho_f}{\mu}I_c\ddot{u}$ in Equation (6), and after that the acceleration of the fluid relative to the solid is taken into account for the mass balance, $\frac{k\rho_f}{\mu n_f}\dot{q}$ in Equation (6). Finally, two separate inertia terms are used to include the relative acceleration in the momentum balance by including $\rho_f I_c^T \dot{q}$ from Equation (4). All simulations have been carried out using the 640×60 mesh, and an intrinsic permeability $k = 10^{-8}$ m^2.
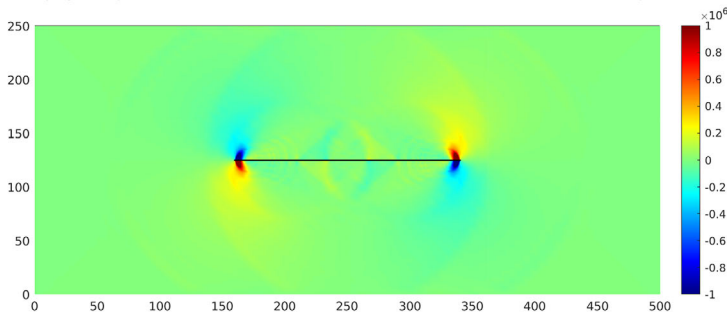
The interstitial fluid pressure that results from these simulations is shown in Figure 2. Without acceleration-driven flow, only slight changes in pressure occur due to the compression of the porous material, as shown in Figure 2(A). These high- and low-pressure regions are diffused over a large area because of the high permeability.
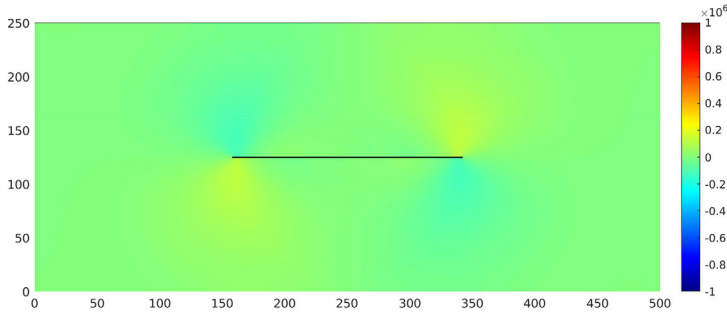
(A) Single inertia terms in momentum balance, no acceleration terms in Darcy's law.
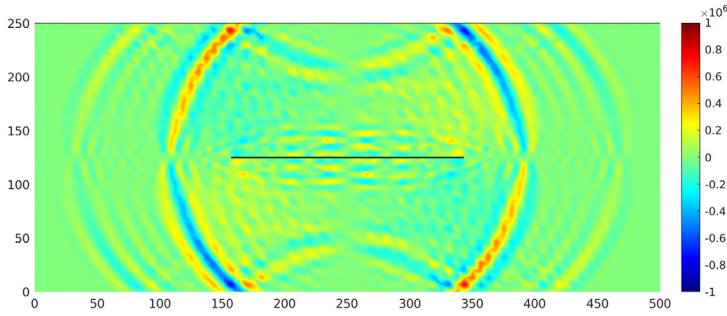
(B) Single inertia terms in momentum balance, only the $\ddot{\boldsymbol{u}}$ term in Darcy's law.
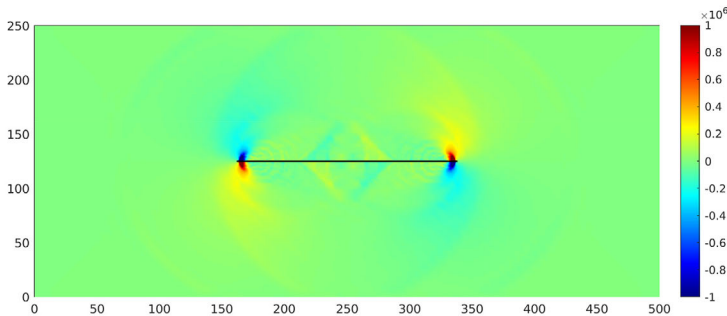
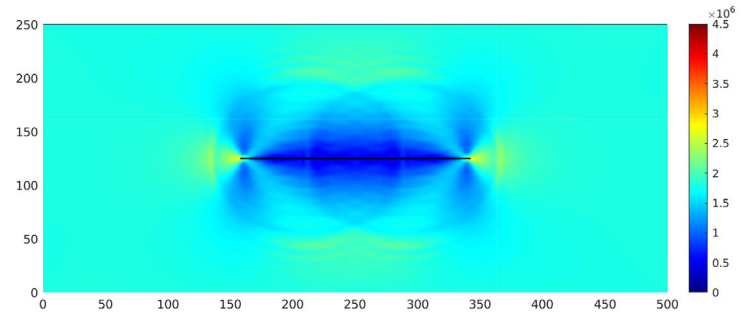(C) Single inertia terms in momentum balance, all terms in Darcy's law.

(D) All terms in Darcy's law and the momentum balance.

FIGURE 2 Interstitial fluid pressure at time $t - t_0 = 52$ ms when different acceleration terms are included in the formulation

Including solid acceleration-driven fluid flow results in the fluid pressure reacting to the acceleration waves in the solid, see Figure 2(B). For the sides of the fracture that are under compression (top right and bottom left), this causes low-pressure regions at the location of the stress waves that originate from the fracture tips, encapsulated by two high-pressure regions that result from the accelerations forcing the fluid away from the stress waves. However, pressure oscillations can be seen throughout the domain due to this coupling between the fluid fluxes and solid acceleration.

Adding the fluid acceleration term in Darcy's law removes these interstitial pressure oscillations, as shown in Figure 2(C). This is a result of the fluid acceleration term adding additional damping to the formulation, thereby decreasing the magnitude of the stress and pressure waves away from the discontinuity. Adding the fluid acceleration term also increases the pressure at the fracture tips, resulting in higher pressures on the compression sides, and lower
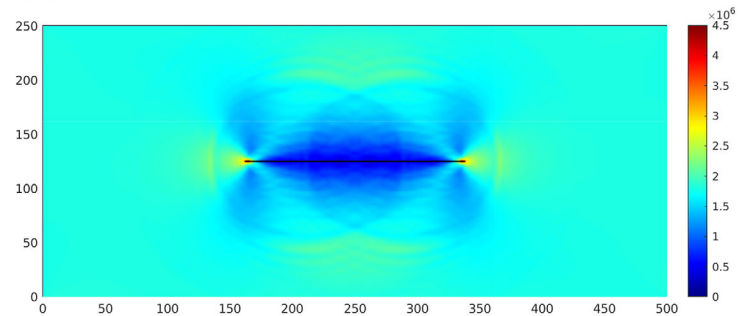
FIGURE 3 Shear stress σ_{yx} at time $t - t_0 = 52$ ms when different acceleration terms are included in the formulation
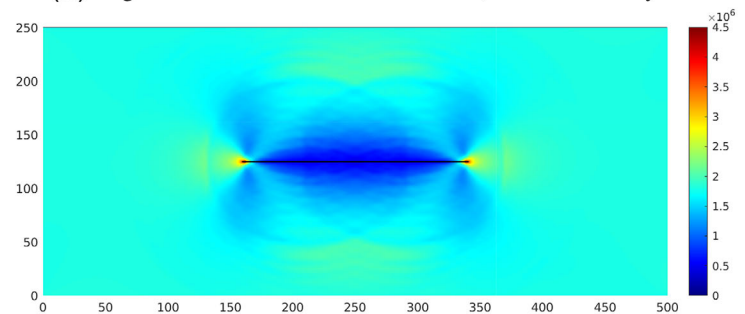

(A) Single inertia terms in momentum balance, no acceleration terms in Darcy's law.
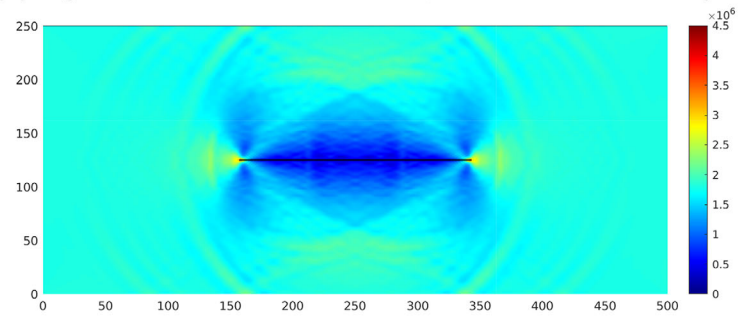
(B) Single inertia terms in momentum balance, only the $\ddot{u}$ term in Darcy's law.

(C) Single inertia terms in momentum balance, all terms in Darcy's law.

(D) All terms in Darcy's law and the momentum balance.

pressures on the extension sides compared to the cases without this term. Finally, using separate inertia terms in the mass balance does not result in any significant changes in the interstitial fluid pressure (Figure 2D).

The shear stress σ_{yx} is shown in Figure 3. Similar to the fluid pressure, slight stress oscillations occur when only the solid acceleration term is included, and disappear if the fluid acceleration term is added. Using separate inertia terms results in slight changes in shear stress, mainly near the center of the domain. However, the effect of the acceleration and separate inertia terms on the shear stress (and other stress components, not shown here) is small compared to the effects on the fluid pressure.

From these results, it can be concluded that the acceleration-driven flow has a significant effect on the fluid pressure, and needs to be included in the formulation. The inclusion of separate inertia terms, however, results in lengthy terms
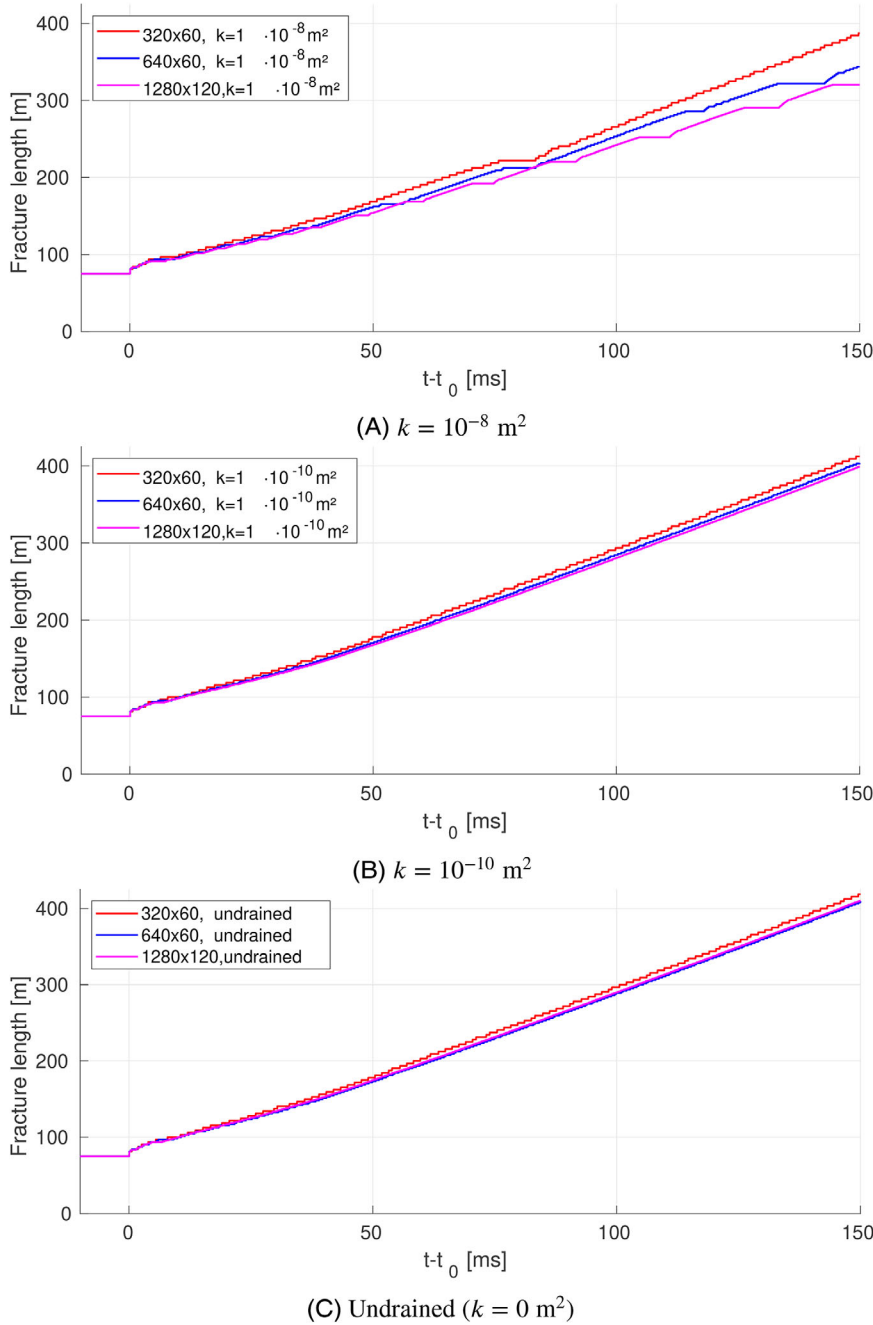
FIGURE 4 Effect of mesh refinement on the fracture propagation

(A) $k = 10^{-8}$ m^2

(B) $k = 10^{-10}$ m^2

(C) Undrained ($k = 0$ m^2)

in the internal force vector, while having near to no effect on the resulting pressures and stresses. In the remainder of this paper, only the acceleration-driven fluid flow terms will therefore be included, while neglecting the effects of using separate inertia terms.
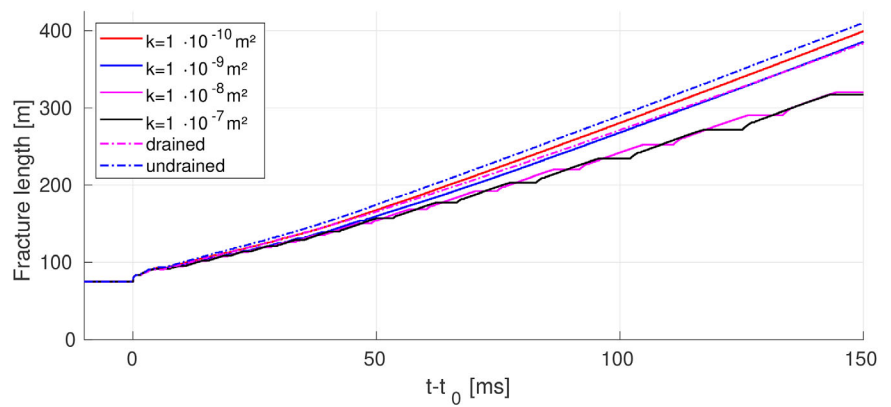
5 | STEPWISE FRACTURE PROPAGATION

5.1 | Mesh refinement

The three different meshes were used to simulate the undrained, the drained, $k = 10^{-8}$ m^2, and $k = 10^{-10}$ m^2 cases to investigate the effect of the interface element size on the fracture propagation. For the drained (not shown), the undrained (Figure 4B), and the $k = 10^{-10}$ m^2 cases, the interface element size does not significantly alter the fracture propagation. With the coarse 320×60 mesh, small steps in the fracture length are seen, with the size of these steps corresponding to

FIGURE 5 Effect of mesh refinement on the fracture propagation using $k = 10^{-8}$ m^2
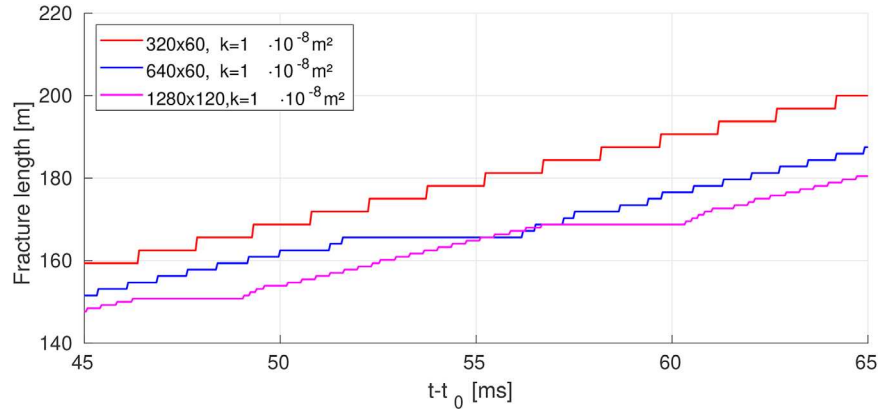
FIGURE 6 Fracture propagation length for different values of the intrinsic permeability

two interface element lengths. These steps originate from the element-wise fracture propagation resulting in a minimum propagation length corresponding to the element size. If the shear stress is not sufficient to fracture a complete element, as evaluated in all the integration points of the interface element, no fracture propagation occurs. Once the stress rises and exceeds the fracture toughness, the complete element fractures at once, resulting in a jump in the fracture length. Due to the symmetry of the simulated cases, this results in either two or no elements fracturing, and thus creating jumps in the fracture length equal to two element lengths. These jumps decrease upon mesh refinement, but do still occur even for the finest mesh as shown in Figure 5. Therefore, this stepwise fracture propagation is solely caused by the spatial and temporal discretization of the problem, and does not originate from a physical phenomenon. It is important to note that if the time step size is increased such that the fracture propagates at least once during each time step, these steps in the fracture propagation will disappear since the propagation is assumed to occur as part of the time step. This is in contrast to fracture propagation schemes that assumes the fracture to propagate in between time steps,[40,41] where these steps will remain independent of the used temporal discretization.

The results for the $k = 10^{-8}$ m^2 case are shown in Figure 4(A). In contrast to the other cases, there is a clear difference between the three meshes. Next to the steps originating from the element size, the coarsest mesh also shows a temporary arrest in the fracture propagation. Upon mesh refinement, these arrests become more common. The finest mesh also shows that the duration of the arrests increases. The difference between this manner of stepwise fracture propagation and the element-sized steps observed for all cases is clearly seen in Figure 5. The small steps occur for all meshes, but the pronounced stick-slip like behavior results in large plateaus when plotting the fracture length as a function of time. While this behavior occurs for all meshes, only the fine meshes resolve the fracture propagation in sufficient detail to distinguish the smaller arrests close to the start of the simulation from the element-wise fracture propagation. Furthermore, while the propagation velocity does not differ between the coarsest and finest mesh, the additional stick-slip behavior results in a significantly slower fracture propagation.
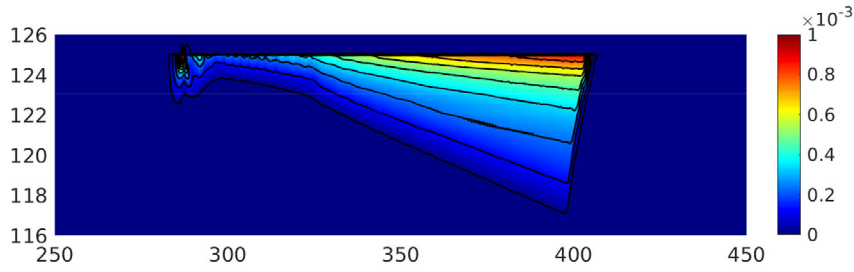
(A) Drained $(p = 0\ Pa)$
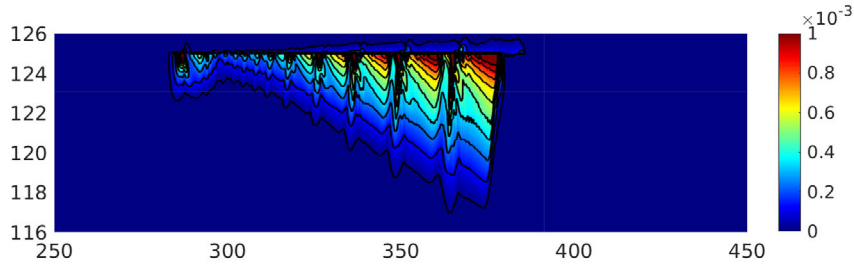
(B) $k = 10^{-7}\ \text{m}^2$
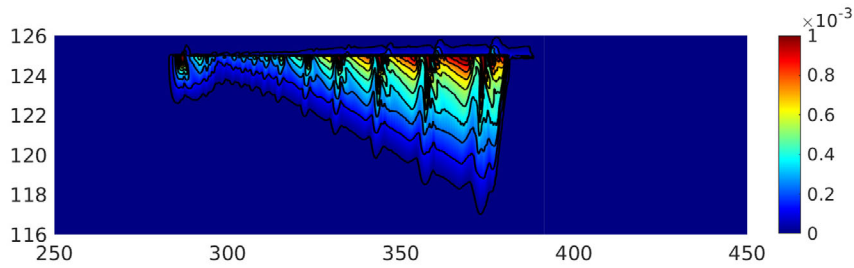
(C) $k = 10^{-8}\ \text{m}^2$
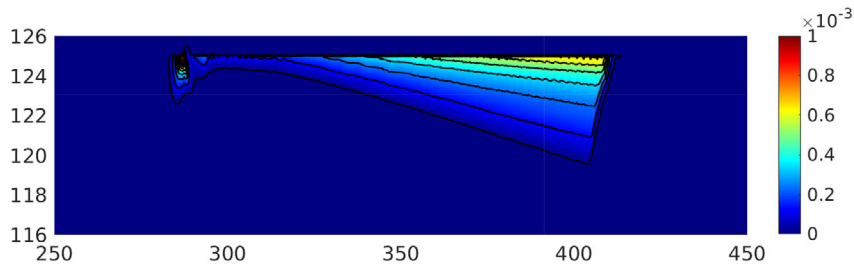
(D) $k = 10^{-10}\ \text{m}^2$
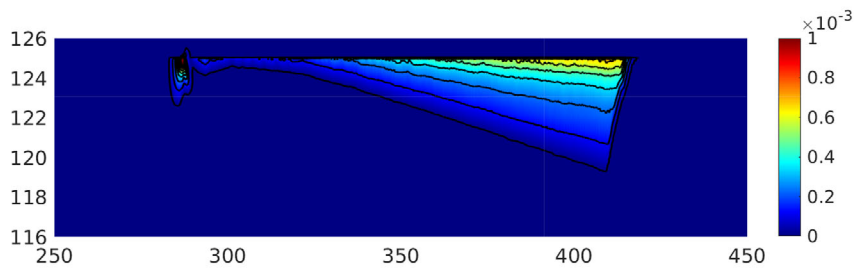
(E) Undrained $(k = 0\ \text{m}^2)$

5.2 | Effect of the permeability

Results for the complete range of permeabilities that have been analyzed are presented in Figure 6 for the 1280×120 mesh. As also shown in the previous section, stick-slip like behavior is observed for the simulations with a high permeability, whereas this does not occur for lower permeabilities, and neither for the drained and undrained cases. Due to the lack of
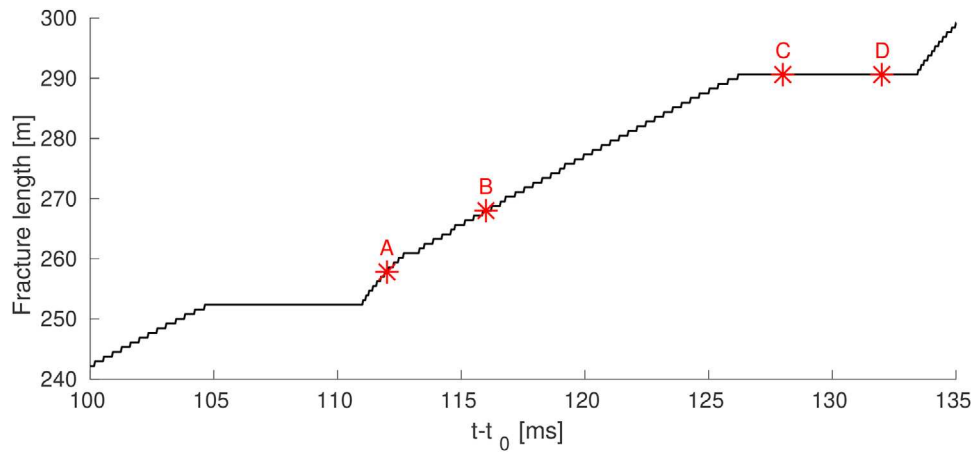
FIGURE 8 Fracture length and location of Figures 9–10 using $k = 10^{-8}$ m^2

stick-slip behavior, the $k = 10^{-10}$ m^{2}case approaches the fracture propagation length of the undrained case, while for high values of the permeability the fracture propagates slower than for the drained case. Relative little difference is seen between $k = 10^{-8}$ m^2 and $k = 10^{-7}$ m^2, suggesting that for these values, the behavior of a highly permeable porous material is approached. This indicates that while the undrained limit is a good approximation for cases with a low permeability, the drained limit neglects important physical phenomena and, accordingly, does not correctly approximate the behavior for high values of the permeability.

The plastic strain near the right fracture at time $t - t_0 = 120$ ms is shown in Figure 7. The undrained and drained cases show a similar behavior as was observed in Ref. 11, with the plasticity being limited to the extensional side of the fracture, and plastic deformations occurring over a larger area for the drained case compared to the undrained case. While the $k = 10^{-10}$ m^2 case approximates the results from the undrained case, the plastic strains obtained for the higher permeability cases differ significantly from the drained case. Large plastic deformation peaks are observed at the locations of the pauses, while more plastic deformation is seen between these pauses. In contrast to the other cases, the higher permeability cases also display a slight amount of plastic deformation on the compression sides of the discontinuity. This further confirms that the high permeability cases do not approach the behavior of the drained limit case.

5.3 | Explanation for stick-slip like fracture propagation

To explain the cause of the stick-slip behavior, we consider the simulation for $k = 10^{-8}$ m^2 at four different times, see Figure 8. The interstitial fluid pressure is given in Figure 9 and the shear stress, causing propagation of the fracture, is shown in Figure 10. When the fracture propagation restarts, there is a large low-pressure region on the compression side next to a small high-pressure region, while the reverse takes place at the extension side (Figure 10A). This small high-pressure region increases in size and attains a maximum during crack propagation, while the low-pressure region detaches and diffuses away from the discontinuity (Figure 10B). Simultaneously, a new low-pressure region emerges behind the growing high-pressure region. Due to the inclusion of the acceleration-driven fluid flow, fluid is transported away from this low-pressure region, further decreasing its pressure, toward the high-pressure region. This allows a build-up of the pressure near the crack tip. Once this region starts to overtake the crack tip (Figure 10C), crack propagation arrests. However, due to the acceleration terms in Darcy's law, the high-pressure region continues to overtake the crack tip (Figure 10D). Only when the high-pressure region above the fracture, and the low-pressure region below it have overtaken the crack tip, fracture propagation is resumed and a new high-pressure region starts to build up behind the crack tip.

The effect of alternatingly building up high- and low-pressure regions influences the shear stresses near the interface, as shown in Figure 10. While the shear stress is concentrated around the crack tip at the beginning of fracture propagation (Figure 10A), the high- and low-pressure regions diffuse this stress over a growing region (Figures 10B and 10C). Once the fracture has arrested, this shear stress is distributed over a significantly larger region compared to the beginning of the fracture propagation. The effect of the pressure overtaking the fracture is also clearly seen in Figure 10(D). Once the
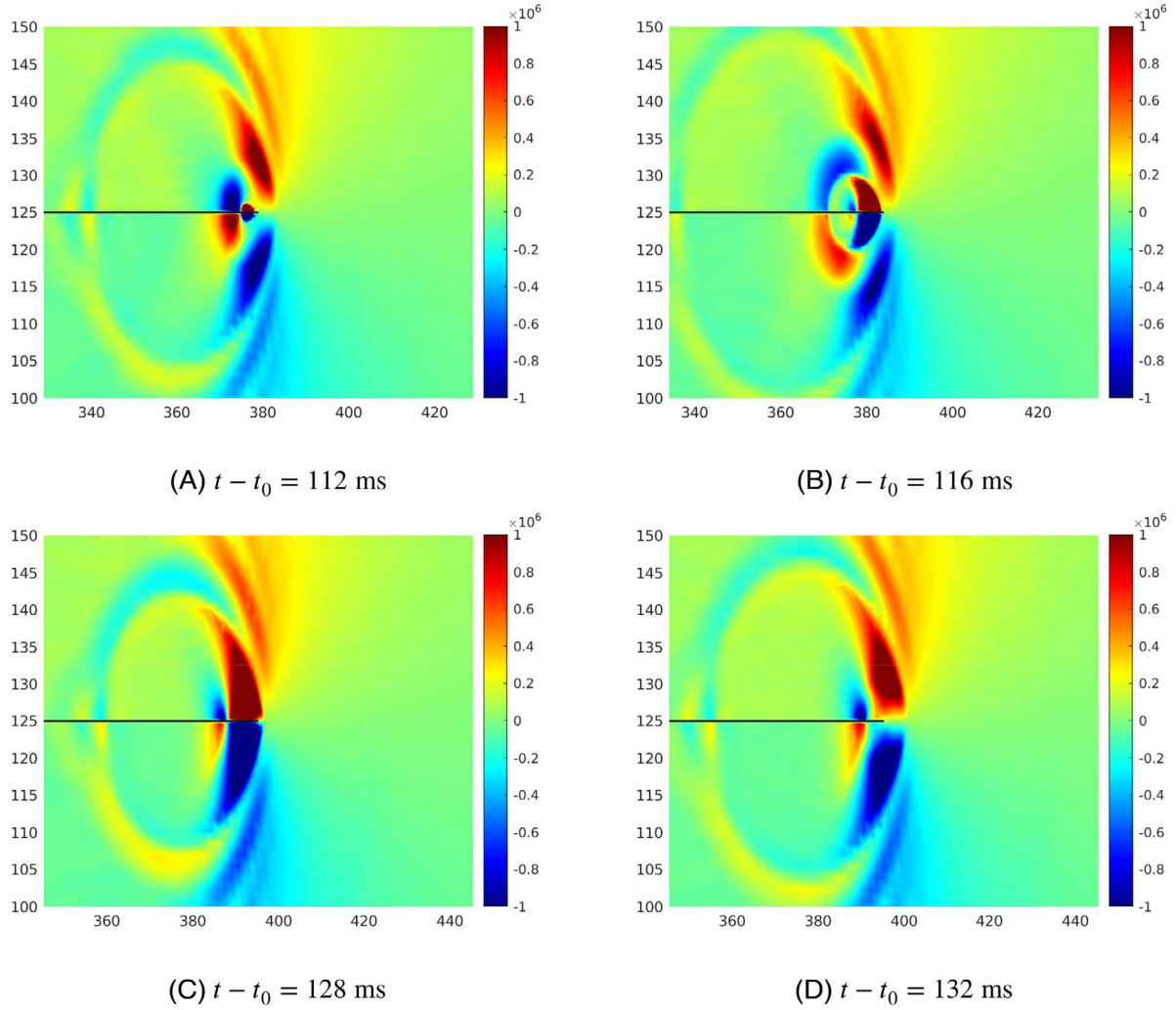
FIGURE 9 Interstitial fluid pressure around the right crack tip for $k = 10^{-8}$ m^2

shear stress concentrations emerge again, as a result of the pressure regions being away from the discontinuity, crack propagation restarts.

Considering the results for a lower permeability (Figure 11) or when the fluid acceleration terms are not included (Figure 12), we observe that these alternating pressure regions do not occur. For the low-permeability case, the acceleration-driven fluid flow terms are small compared to the pressure changes induced by the compression of the porous material. The shear stresses are also concentrated near the fracture tip for both these cases, in contrast to the case with a high permeability, where these stresses diffused over a larger region. This shows that the stick-slip like behavior is purely caused by the acceleration-driven fluid flow, and that excluding acceleration-driven fluid flow terms significantly alters the crack propagation.

6 | SUPERCRITICAL SHEAR FRACTURE PROPAGATION

A second case is now considered with a combination of external forces to cause the propagation velocity of the fracture to exceed the shear wave speed. Now $t_{xx} = 19$ MPa, $t_{yy} = 10$ MPa, $t_{xy} = t_{yx} = 2.4$ MPa, while all everything else corresponds to the previous case study, Section 3.

The crack velocity, obtained using the 1280×120 mesh, is shown in Figure 13(A). Different from the previous case, no stick-slip like behavior occurs. Furthermore, the simulations for different values of the permeability all approach the undrained case, while the crack in the drained case propagates slightly slower. This can be explained by considering the interstitial fluid pressure in Figure 14. The simulation for $k = 10^{-8}$ m^2 still results in a high-pressure region next to

(A) $t - t_0 = 112$ ms

(B) $t - t_0 = 116$ ms

(C) $t - t_0 = 128$ ms

(D) $t - t_0 = 132$ ms
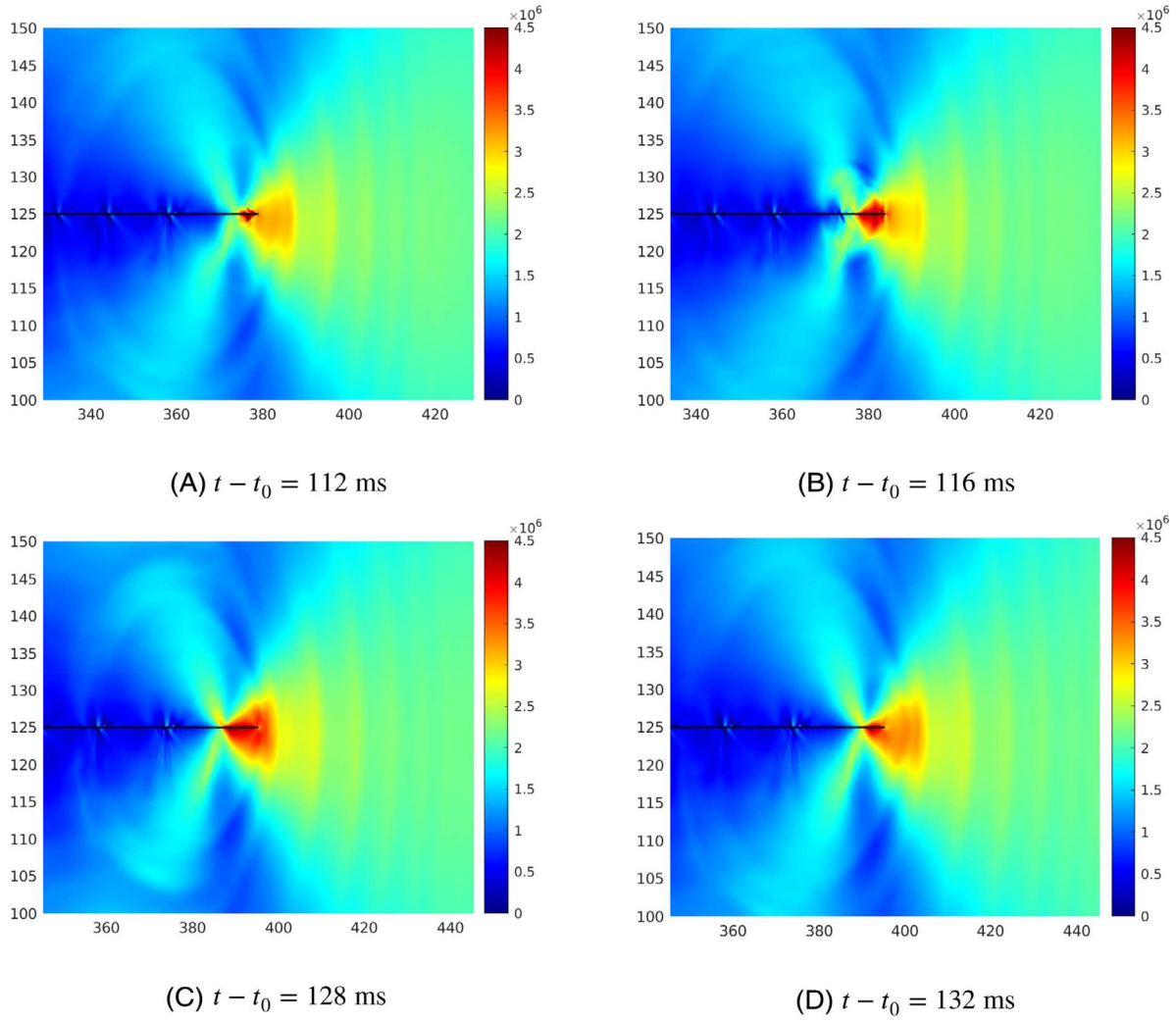
FIGURE 10 Shear stress σ_{yx} around the right crack tip for $k = 10^{-8}$ m^2

(A) Interstitial fluid pressure
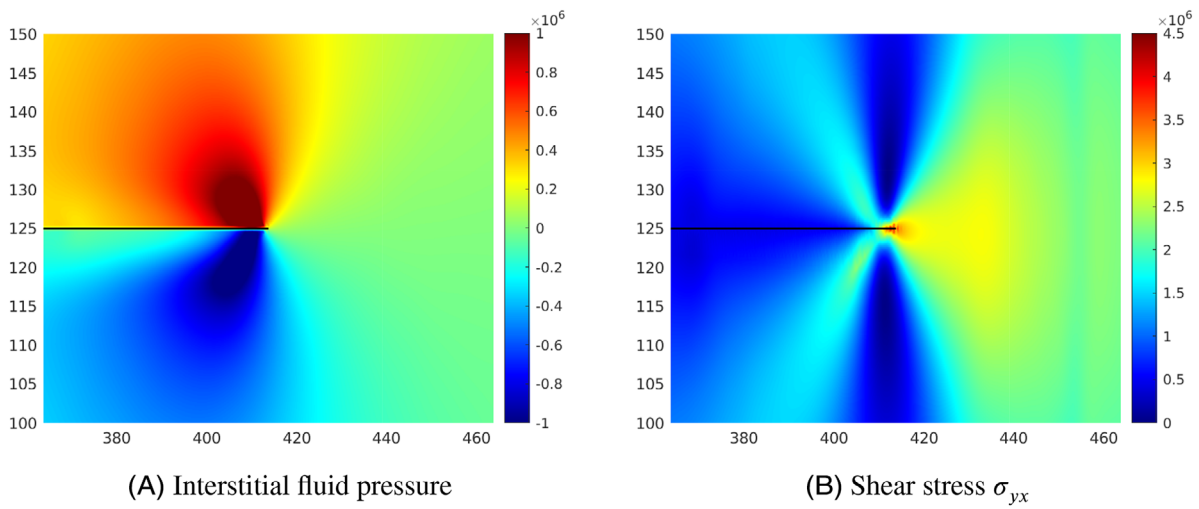
(B) Shear stress σ_{yx}

FIGURE 11 Interstitial fluid pressure and shear stress around the right crack tip for $k = 10^{-10}$ m^2 at $t - t_0 = 120$ ms

(A) Interstitial fluid pressure
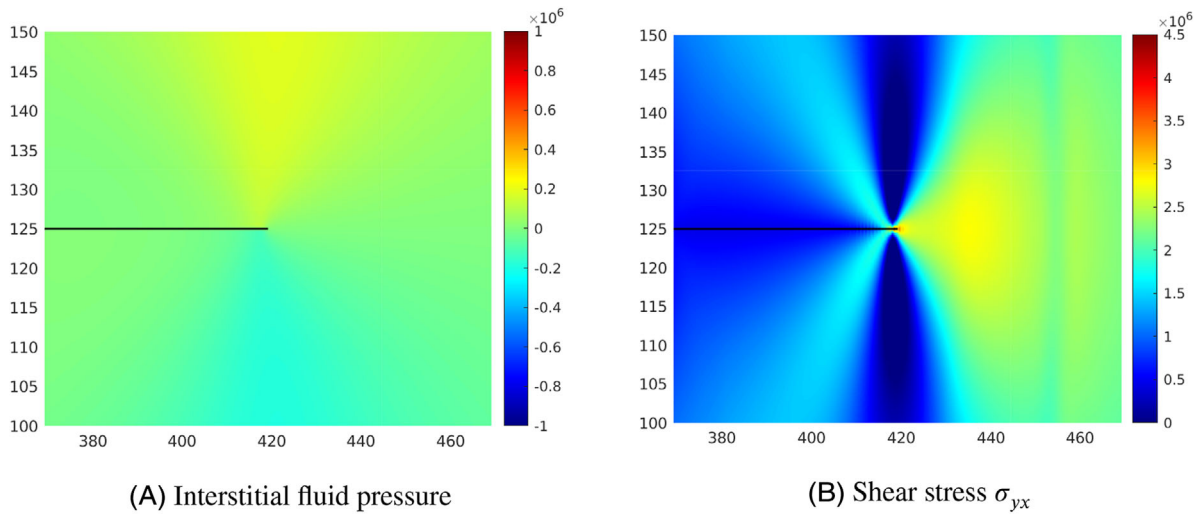
(B) Shear stress σ_{yx}

FIGURE 12 Interstitial fluid pressure and shear stress around the right fracture tip for $k = 10^{-8}$ m^2 without acceleration terms in Darcy's law $t - t_0 = 120$ ms
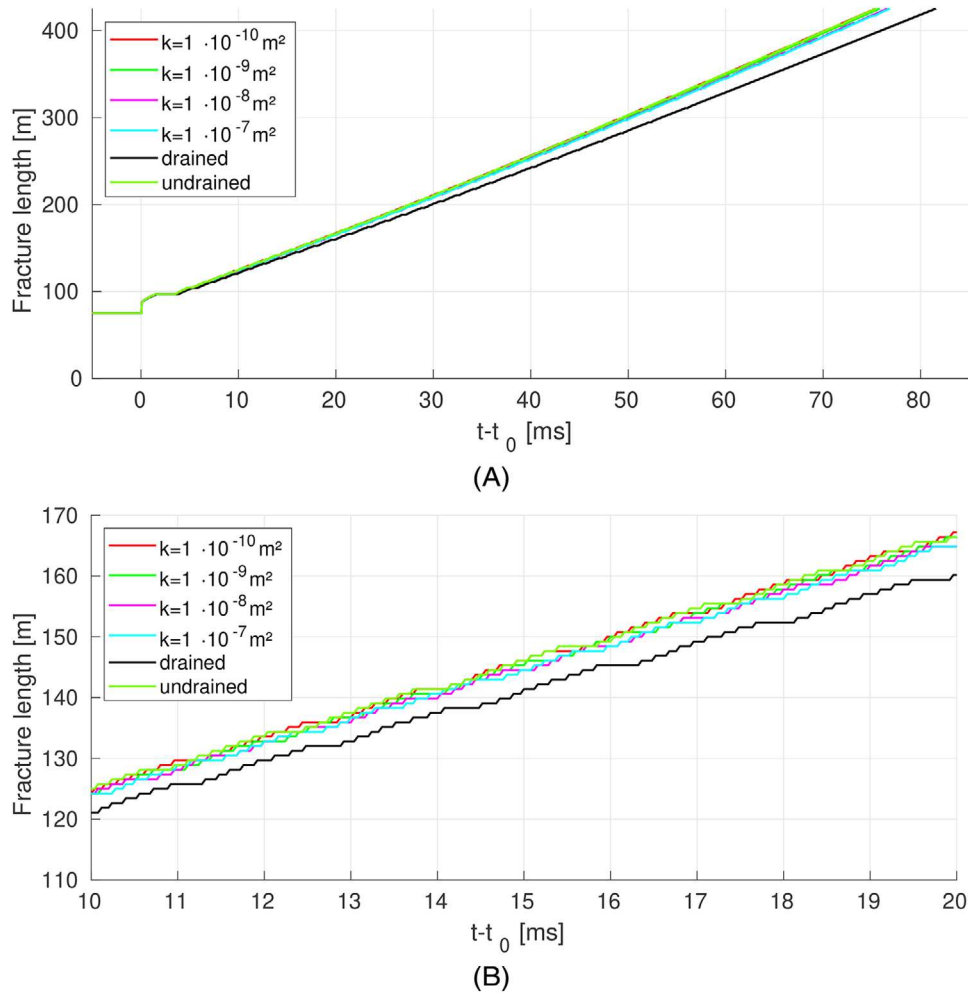

(A)

(B)

FIGURE 13 Fracture length for varying permeability using the altered external load
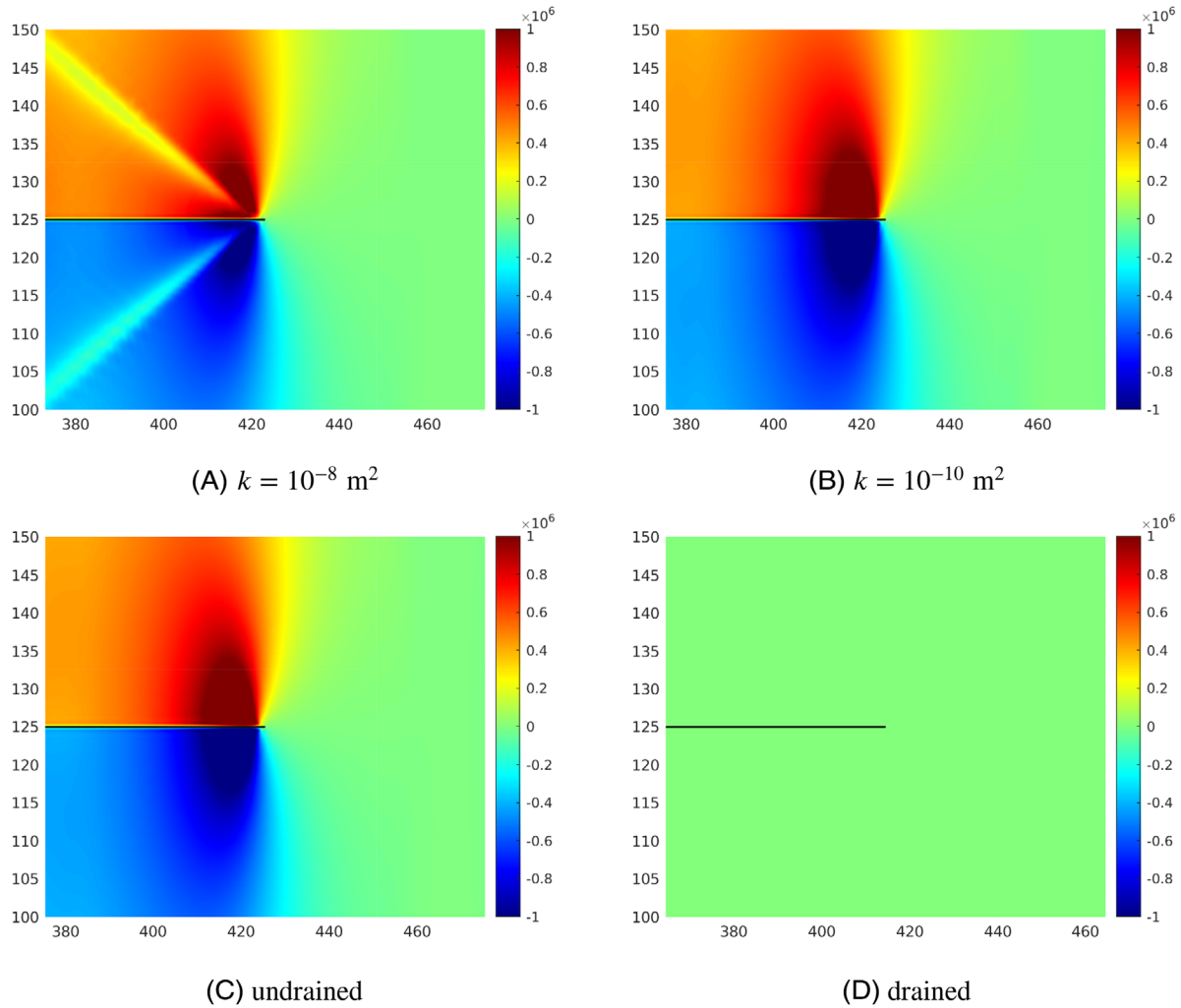
FIGURE 14 Interstitial fluid pressure around the right fracture tip at $t - t_0 = 60$ ms

a low-pressure region on the compressive side of the fracture. However, due to the high propagation velocity, this high-pressure region cannot overtake the fracture tip, and therefore, the interstitial fluid pressure does not initiate the stick-slip behavior observed before. Comparing the results for $k = 10^{-8}$ m^2, $k = 10^{-10}$ m^2 and the undrained case also shows why the propagation velocity is similar in those cases. No interstitial fluid pressure is present in front of the fracture, whereas the combination of acceleration-driven fluid flow (for the high-permeability case) and compression of the porous material results in similar pressures just behind the fracture tip.

While no stick-slip behavior originating from the interstitial fluid pressure is observed, small arrests in the crack propagation still occur for all cases, see Figure 13(B). They are independent of the value of the permeability, and only occur up to $t - t_0 \approx 40$ ms (corresponding to a fracture from $x = 125-375$ m). Thereafter, arrests are no longer observed, only elementwise fracture propagation. The cause of these small arrests lies in the shear stress (Figure 15). Before the onset of fracture propagation, the domain is in equilibrium. However, once propagation occurs, it happens faster than the shear stress can react, resulting in the fracture propagating through the initially present shear stress and causing oscillations. These oscillations are responsible for the short arrests. Eventually, the fracture exits the region that was influenced by the initial position of the fracture and these stress oscillations disappear.

7 | CONCLUDING REMARKS

A pressure–displacement formulation has been presented for fluid-saturated porous media that includes acceleration-driven fluid flow and separate inertia terms. It has been shown that these acceleration-driven flow terms can have a

][!ht]

(A) $t - t_0 = 0$ ms

(B) $t - t_0 = 4$ ms

(C) $t - t_0 = 12$ ms

(D) $t - t_0 = 20$ ms

(E) $t - t_0 = 28$ ms

(F) $t - t_0 = 32$ ms
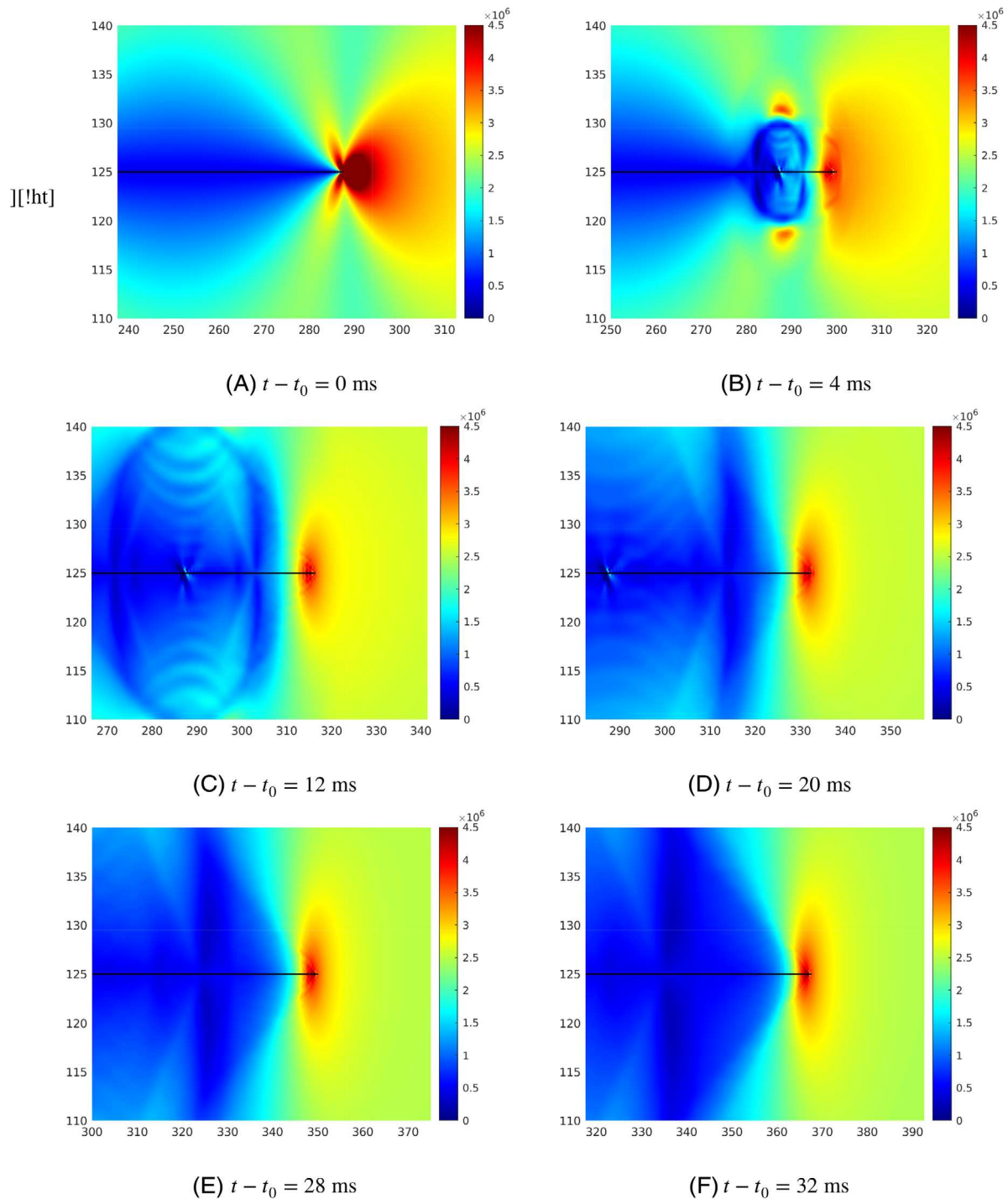
FIGURE 15 Shear stress around the right fracture tip using $k = 10^{-8}$ m^2

significant impact. Including the solid acceleration results in the interstitial fluid pressure reacting to the pressure and the shear stress waves, but also causes oscillations in the interstitial fluid pressure. Adding the fluid acceleration adds extra damping, removing these oscillations and limiting changes in fluid pressure away from the source of the stress waves. The fluid acceleration term is also responsible for causing small high- and low-pressure regions near the fracture tip. Finally, simulations using separate inertia terms for the fluid and solid show near to no effect of using these separate inertia terms.

Simulations of a shear fracture in a porous material with varying permeability show several types of stepwise fracture propagation. The first type of stepwise fracture propagation is related to the elementwise fracture propagation, and

was shown to gradually vanish upon mesh refinement. These steps originate from the small time step used during these simulations, causing either zero or two elements to fracture. This necessitates small time steps. This type of stepwise propagation shows a consistent pattern of very short arrests followed by a jump in fracture length equal to a single element (or two-element lengths in case of symmetric problems). This type of stepwise propagation is a numerical artifact, and does not have a physical origin.

The second type of stepwise propagation observed was a stick-slip like behavior that originates from the acceleration-driven fluid flow. This results in alternating high- and low-pressure regions near the fracture tip, arresting the fracture propagation once one of these regions starts to overtake the fracture tip. This stick-slip like behavior could be observed only when a sufficiently fine mesh was employed, and only occurred for simulations using a high value of the permeability, so that the acceleration terms could dictate the changes in interstitial fluid pressure.

Finally, simulations have been carried out using a combination of external forces that resulted in a crack propagation velocity exceeding the shear wave speed. For these simulations, the interstitial fluid pressure build-up is unable to overtake the fracture, and therefore, the second type of stepwise propagation does not occur. However, a third type of stepwise propagation was observed, originating from the initial conditions not adapting fast enough to the propagating fracture. The fast fracture propagation resulted in stress oscillations when propagating through the initial stress, with these stress oscillations causing small arrests in the fracture propagation. These arrests disappear once the fracture exits the region influenced by the initial stress field.

CONFLICT OF INTEREST
The authors declare that there is no conflict of interest regarding the publication of this paper.

DATA AVAILABILITY STATEMENT
Data sharing is not applicable to this article as no datasets were generated or analyzed during the current study.

ORCID
Tim Hageman https://orcid.org/0000-0001-7770-7440
René de Borst https://orcid.org/0000-0002-3457-3574

REFERENCES
1. Zbinden D, Rinaldi AP, Urpi L, Wiemer S. On the physics-based processes behind production-induced seismicity in natural gas fields. *J Geophys Res: Solid Earth*. 2017;122:3792-3812.
2. French ME, Zhu W, Banker J. Fault slip controlled by stress path and fluid pressurization rate. *Geophys Res Lett*. 2016;43:4330-4339.
3. Myake Y, Noda H. Fully dynamic earthquake sequence simulation of a fault in a viscoelastic medium using a spectral boundary integral equation method: does interseismic stress relaxation promote aseismic transients? *Earth Planets Space*. 2019;71:137.
4. Chang KW, Segall P. Injection-induced seismicity on basement faults including poroelastic stressing. *J Geophys Res: Solid Earth*. 2016;121(4):2708-2726.
5. Ougier-Simonin A, Zhu W. Effects of pore fluid pressure on slip behaviors: an experimental study. *Geophys Res Lett*. 2013;40:2619-2624.
6. Scuderi MM, Collettini C, Marone C. Frictional stability and earthquake triggering during fluid pressure stimulation of an experimental fault. *Earth Planet Sci Lett*. 2017;477:84-96.
7. Segall P, Lu S. Injection-induced seismicity: poroelastic and earthquake nucleation effects. *J Geophys Res: Solid Earth*. 2015;120:5082-5103.
8. Galis M, Pelties C, Kristek J, Moczo P, Ampuero JP, Mai PM. On the initiation of sustained slip-weakening ruptures by localized stresses. *Geophys J Int*. 2015;200:890-909.
9. Galis M, Ampuero JP, Mai PM, Cappa F. Induced seismicity provides insight into why earthquake ruptures stop. *Sci Adv*. 2017;3:eaap7528.
10. Templeton EL, Rice JR. Off-fault plasticity and earthquake rupture dynamics: 1. Dry materials or neglect of fluid pressure changes. *J Geophys Res: Solid Earth*. 2008;113(9):B09306.
11. Viesca RC, Templeton EL, Rice JR. Off-fault plasticity and earthquake rupture dynamics: 2. Effects of fluid saturation. *J Geophys Res*. 2008;113(B9):B09307.
12. Hirakawa E, Ma S. Dynamic fault weakening and strengthening by gouge compaction and dilatancy in a fluid-saturated fault zone. *J Geophys Res: Solid Earth*. 2016;121(8):5988-6008.
13. Hirakawa E, Ma S. Undrained gouge plasticity stabilizes rupture dynamics of rough faults. *Bull Seismol Soc Am*. 2018;108:3160-3168.
14. Cappa F. Influence of hydromechanical heterogeneities of fault zones on earthquake ruptures. *Geophys J Int*. 2011;185:1049-1058.

15. Jin L, Zoback MD. Fully dynamic spontaneous rupture due to quasi-static pore pressure and poroelastic effects: an implicit nonlinear computational model of fluid-induced seismic events. *J Geophys Res: Solid Earth*. 2018;123(11):9430-9468.

16. Garagash DI, Germanovich LN. Nucleation and arrest of dynamic slip on a pressurized fault. *J Geophys Res B: Solid Earth*. 2012;117(10):1-27.

17. Zienkiewicz OC, Chang CT, Bettess P. Drained, undrained, consolidating and dynamic behaviour assumptions in soils. *Géotechnique*. 1980;30:385-395.

18. Zienkiewicz OC, Chan AHC, Paston M, Schrefler BA, Shiomi T. *Computational Geomechanics – With Special Reference to Earthquake Engineering*. Chichester: John Wiley & Sons; 1999. correct reference

19. de Borst R. *Computational Methods for Fracture in Porous Media*. New York: Elsevier; 2017. Correct reference.

20. Monforte L, Navas P, Carbonell JM, Arroyo M, Gens A. Low-order stabilized finite element for the full Biot formulation in soil mechanics at finite strain. *Int J Numer Analyt Methods Geomech*. 2019;43:1488-1515.

21. Bardet JP. The damping of saturated poroelastic soils during steady-state vibrations. *Appl Math Comput*. 1995;67:3-31.

22. Qiu T, Fox PJ. Numerical analysis of 1-D compression wave propagation in saturated poroelastic media. *Int J Numer Analyt Methods Geomech*. 2008;32:161-187.

23. Qiu T, Huang Y. Energy dissipation in nearly saturated poroviscoelastic soil columns during quasi-static compressional excitations. *J Eng Mech*. 2012;138:1263-1274.

24. Loret B, Radi E. The effects of inertia on crack growth in poroelastic fluid-saturated media. *J Mech Phys Solids*. 2001;49:995-1020.

25. Zhang Y, Pedroso DM, Ehlers W. One-dimensional dynamics of saturated incompressible porous media: analytical solutions and influence of inertia terms. *Int J Numer Analyt Methods Geomech*. 2016;40:2489-2513.

26. Secchi S, Schrefler BA. Hydraulic fracturing and its peculiarities. *Asia Pac J Comput Eng*. 2014;1:8.

27. Milanese E, Yllmaz O, Molinari JF, Schrefler BA. Avalanches in dry and saturated disordered media at fracture. *Phys Rev E*. 2016;93:043002.

28. Milanese E, Cao TD, Simoni L, Schrefler BA. Fracturing in dry and saturated porous media. *Comput Methods Appl Sci*. 2018;46:265-288.

29. Peruzzo C, Simoni L, Schrefler BA. On stepwise advancement of fractures and pressure oscillations in saturated porous media. *Eng Fract Mech*. 2019;215:246-250.

30. Zhang GQ, Chen M. Dynamic fracture propagation in hydraulic re-fracturing. *J Petrol Sci Eng*. 2010;70:266-272.

31. Pizzocolo F, Huyghe JM, Ito K. Mode I crack propagation in hydrogels is step wise. *Eng Fract Mech*. 2013;97:72-79.

32. Dong J, Chen M, Li Y, Wang S, Zeng C, Zaman M. Experimental and theoretical study on dynamic hydraulic fracture. *Energies*. 2019;12:397.

33. Bhattacharya P, Viesca RC. Fluid-induced aseismic fault slip outpaces pore-fluid migration. *Science*. 2019;364(6439):464-468.

34. Beroza GC, Ide S. Slow earthquakes and nonvolcanic tremor. *Annu Rev Earth Planet Sci*. 2011;39:271-296.

35. Feng Y, Gray KE. Parameters controlling pressure and fracture behaviors in field injectivity tests: a numerical investigation using coupled flow and geomechanics model. *Comput Geotech*. 2017;87:49-61.

36. Nguyen VP, Lian H, Rabczuk T, Bordas S. Modelling hydraulic fractures in porous media using flow cohesive interface elements. *Eng Geol*. 2017;225:68-82.

37. Tzschichholz F, Herrmann HJ. Simulations of pressure fluctuations and acoustic emission in hydraulic fracturing. *Phys Rev E*. 1995;51:1961-1970.

38. Mohammadnejad T, Khoei AR. Hydro-mechanical modeling of cohesive crack propagation in multiphase porous media using the extended finite element method. *Int J Numer Analyt Methods Geomech*. 2013;37:1247-1279.

39. Pervaiz Fathima KM, de Borst R. Implications of single or multiple pressure degrees of freedom at fractures in fluid-saturated porous media. *Eng Fract Mech*. 2019;213:1-20.

40. Cao TD, Milanese E, Remij EW, et al. Interaction between crack tip advancement and fluid flow in fracturing saturated porous media. *Mech Res Commun*. 2017;80:24-37.

41. Cao TD, Hussain F, Schrefler BA. Porous media fracturing dynamics: stepwise crack advancement and fluid pressure oscillations. *J Mech Phys Solids*. 2018;111:113-133.

42. Ni T, Pesavento F, Zaccariotto M, Galvanetto U, Zhu QZ, Schrefler BA. Hybrid FEM and peridynamic simulation of hydraulic fracture propagation in saturated porous media. *Comput Methods Appl Mech Eng*. 2020;366:113101.

43. Remij EW, Remmers JJC, Huyghe JM, Smeulders DMJ. An investigation of the step-wise propagation of a mode-II fracture in a poroelastic medium. *Mech Res Commun*. 2017;80:10-15.

44. Cosserat E, Cosserat F. *Théorie des Corps Deformables*. Paris: A. Hermann & Fils; 1909. Correct reference.

45. de Borst R. A generalisation of J2-flow theory for polar continua. *Comput Methods Appl Mech Eng*. 1993;103:347-362.

46. Sabet SA, de Borst R. Mesh bias and shear band inclination in standard and non-standard continua. *Arch Appl Mech*. 2019;89:2577-2590.

47. Sabet SA, de Borst R. Structural softening, mesh dependence, and regularisation in non-associated plastic flow. *Int J Numer Analyt Methods Geomech*. 2019;43:2170-2183.

48. de Borst R, Sluys LJ. Localisation in a Cosserat continuum under static and dynamic loading conditions. *Comput Methods Appl Mech Eng*. 1991;90:805-827.

49. de Borst R. Simulation of strain localization: a reappraisal of the Cosserat continuum. *Eng Comput*. 1991;8:317-332.

50. Hageman T, Sabet SA, de Borst R. Convergence in non-associated plasticity and fracture propagation for standard, rate-dependent and Cosserat continua. *Int J Numer Methods Eng*. 2020;122:777-795.

51. Schrefler BA, Scotta R. A fully coupled dynamic model for two-phase fluid flow in deformable porous media. *Comput Methods Appl Mech Eng*. 2001;190:3223-3246.

52. Réthoré J, de Borst R, Abellan M-A. A discrete model for the dynamic propagation of shear bands in a fluid-saturated medium. *Int J Numer Analyt Methods Geomech*. 2007;31:347-370.

53. Khoei AR, Mohammadnejad T. Numerical modeling of multiphase fluid flow in deforming porous media: a comparison between two- and three-phase models for seismic analysis of earth and rockfill dams. *Comput Geotech*. 2011;38:142-166.

54. Mühlhaus HB, Vardoulakis I. The thickness of shear bands in granular materials. *Géotechnique*. 1987;37:271-283.

55. Palmer AC, Rice JR. The growth of slip surfaces in the progressive failure of over-consolidated clay. *Proc R Soc A: Math Phys Eng Sci*. 1973;332:527-548.

56. Remij EW, Remmers JJC, Huyghe JM, Smeulders DMJ. The enhanced local pressure model for the accurate analysis of fluid pressure driven fracture in porous materials. *Compu Methods Appl Mech Eng*. 2015;286:293-312.

57. de Borst R. Fluid flow in fractured and fracturing porous media: a unified view. *Mech Res Commun*. 2017;80:47-57.

58. Kame N, Rice JR, Dmowska R. Effects of prestress state and rupture velocity on dynamic fault branching. *J Geophys Res: Solid Earth*. 2003;108(B5).

59. Bazilevs Y, Calo VM, Cottrell JA, et al. Isogeometric analysis using T-splines. *Comput Methods Appl Mech Eng*. 2010;199:229-263.

60. Scott MA, Li X, Sederberg TW, Hughes TJR. Local refinement of analysis-suitable T-splines. *Comput Methods Appl Mech Eng*. 2012;213-216:206-222.

61. Irzal F, Remmers JJC, Verhoosel CV, de Borst R. Isogeometric finite element analysis of poroelasticity. *Int J Numer Analyt Methods Geomech*. 2013;37:1891-1907.

62. Hageman T, de Borst R. Flow of non-Newtonian fluids in fractured porous media: isogeometric vs standard finite element discretisation. *Int J Numer Analyt Methods Geomech*. 2019;43:2020-2037.

63. Scott MA, Borden MJ, Verhoosel CV, Sederberg TW, Hughes TJR. Isogeometric finite element data structures based on Bézier extraction of T-splines. *Int J Numer Methods Eng*. 2011;88:126-156.

64. Chapelle D, Bathe KJ. The inf-sup test. *Comput Struct*. 1993;47:537-545.

65. Verhoosel CV, Scott MA, de Borst R, Hughes TJR. An isogeometric approach to cohesive zone modeling. *Int J Numer Methods Eng*. 2011;87:336-360.

66. Vignollet J, May S, de Borst R. On the numerical integration of isogeometric interface elements. *Int J Numer Methods Eng*. 2015;102(11):1733-1749.

67. Irzal F, Remmers JJC, Verhoosel CV, de Borst R. An isogeometric analysis Bézier interface element for mechanical and poromechanical fracture problems. *Int J Numer Methods Eng*. 2014;97:608-628.

68. Chen L, Verhoosel CV, de Borst R. Discrete fracture analysis using locally refined T-splines. *Int J Numer Methods Eng*. 2018;116:117-140.

69. Hageman T, Pervaiz Fathima KM, de Borst R. Isogeometric analysis of fracture propagation in saturated porous media due to a pressurised non-Newtonian fluid. *Comput Geotechn*. 2019;112:272-283.

70. Schellekens JCJ, de Borst R. On the numerical integration of interface elements. *Int J Numer Methods Eng*. 1993;36:43-66.

71. Lysmer J, Kuhlemeyer RL. Finite dynamic model for infinite media. *J Eng Mech Div*. 1969;95:859-878.

APPENDIX A: SYSTEM MATRICES

The discretized equations are solved using a monolithic Newton–Raphson scheme, calculating the iterative increments through:

$$
\begin{bmatrix}
\boldsymbol{K} + \boldsymbol{M} + \boldsymbol{K}_d + \boldsymbol{K}_{ext} & \boldsymbol{Q}_s + \boldsymbol{M}_f & \boldsymbol{Q}_d \\
\boldsymbol{Q}_f + \boldsymbol{A}_s & \boldsymbol{C}_f + \boldsymbol{H} + \boldsymbol{H}_d & \boldsymbol{H}_{dd} \\
\boldsymbol{0} & \boldsymbol{H}_{dd}^T & \boldsymbol{H}_{df}
\end{bmatrix}
\begin{bmatrix}
\mathrm{d}\boldsymbol{u} \\
\mathrm{d}\boldsymbol{p} \\
\mathrm{d}\boldsymbol{p}_d
\end{bmatrix}
=
\begin{bmatrix}
\boldsymbol{f}_{ext} \\
\boldsymbol{q}_{ext} \\
\boldsymbol{0}
\end{bmatrix}
-
\begin{bmatrix}
\boldsymbol{f}_{int} + \boldsymbol{f}_d \\
\boldsymbol{q}_{int} + \boldsymbol{q}_d \\
\boldsymbol{q}_{d,int}
\end{bmatrix}
\tag{A.1}
$$

with the submatrices for the momentum balance given by:

$$
\boldsymbol{K} = \int_\Omega \boldsymbol{B}^T \boldsymbol{D}_{eff} \boldsymbol{B} \, \mathrm{d}\Omega,
\tag{A.2}
$$

$$
\boldsymbol{M} = \int_\Omega \frac{1}{\beta \Delta t^2} \boldsymbol{N}_s^T \left(\bar{\boldsymbol{\rho}} - A n_f \boldsymbol{\rho}_f \right) \boldsymbol{N}_s \, \mathrm{d}\Omega,
\tag{A.3}
$$

$$\boldsymbol{K}_d = \int_{\Gamma_d} \boldsymbol{N}_s^T \boldsymbol{R}^T \boldsymbol{D}_i \boldsymbol{R} \boldsymbol{N}_s + \boldsymbol{N}_s^T \boldsymbol{R}^T \boldsymbol{D}_{czm} \boldsymbol{R} \boldsymbol{N}_s \ d\Gamma_d, \tag{A.4}$$

$$\boldsymbol{K}_{ext} = \int_{\Gamma} \frac{\gamma}{\beta \Delta t} \boldsymbol{N}_s^T \boldsymbol{R}^T \boldsymbol{S} \boldsymbol{R} \boldsymbol{N}_s \ d\Gamma, \tag{A.5}$$

$$\boldsymbol{Q}_s = -\int_{\Omega} \alpha \boldsymbol{B}^T \boldsymbol{m} \boldsymbol{N}_f \ d\Omega, \tag{A.6}$$

$$\boldsymbol{M}_f = -\int_{\Omega} A n_f \boldsymbol{N}_s^T \boldsymbol{I}_c \nabla \boldsymbol{N}_f^T \ d\Omega, \tag{A.7}$$

$$\boldsymbol{Q}_d = -\int_{\Gamma_d} \boldsymbol{N}_s^T \boldsymbol{n}_{\Gamma_d} \boldsymbol{N}_{df} \ d\Gamma_d, \tag{A.8}$$

and the effective stiffness matrix obtained by first inverting

$$\boldsymbol{C}_{eff} = \begin{bmatrix} \boldsymbol{I} + \Delta \lambda_j \boldsymbol{D}_e \frac{\partial^2 g}{\partial \sigma_j^2} & \boldsymbol{D}_e \frac{\partial g}{\partial \sigma_j} \\ \left(\frac{\partial f}{\partial \sigma_j} \right)^T & -\frac{\eta \sigma_0}{\Delta t} \end{bmatrix},$$

then selecting the upper left 7×7 submatrix, and multiplying the result with the linear-elastic stiffness D_e.

The matrix that contains the dummy stiffness values used to prevent a negative fracture opening reads:

$$\boldsymbol{D}_i = \begin{bmatrix} d_n & 0 & 0 \\ 0 & 0 & 0 \\ 0 & 0 & d_\omega \end{bmatrix}.$$

If the history variable is larger than the current tangential displacement, then the tangential stiffness component is given by:

$$D_{czm}(t,n) = -f_r d_n + (f_p - f_r) \exp\left(-2[\![dx]\!]/D_c\right)\left(-d_n + d_n[\![u_n]\!] \cdot 2[\![dx]\!]/D_c^2 \cdot 2\mathcal{G}_c/\left((f_p - f_r)d_n[\![u_n]\!]^2\right)\right).$$

Otherwise, the nonzero components read:

$$D_{czm}(t,t) = 2(f_p - f_r)d_n[\![u_n]\!]/D_c \exp\left(-2[\![u_t]\!]/D_c\right)$$

$$D_{czm}(t,n) = -f_r d_n + (f_p - f_r) \exp\left(-2[\![u_t]\!]/D_c\right)\left(-d_n + d_n[\![u_n]\!] \cdot 2[\![u_t]\!]/D_c^2 \cdot 2\mathcal{G}_c/\left((f_p - f_r)d_n[\![u_n]\!]^2\right)\right).$$

The submatrices related to the mass balances of the porous material and the fracture are given by:

$$\boldsymbol{Q}_f = -\int_{\Omega} \frac{\alpha \gamma}{\beta} \boldsymbol{N}_f^T \boldsymbol{I}_c \boldsymbol{B} \ d\Omega, \tag{A.9}$$

$$\boldsymbol{C}_f = -\int_{\Omega} \frac{1}{M\theta} \boldsymbol{N}_f^T \boldsymbol{N}_f \ d\Omega, \tag{A.10}$$

$$\boldsymbol{A}_s = -\int_{\Omega} \frac{k\rho_f}{\mu \Delta t \beta} \left(1 + \frac{\rho_f k}{n_f \mu \theta \Delta t}\right)^{-1} (\nabla \boldsymbol{N}_f)^T \boldsymbol{I}_c \boldsymbol{N}_s \ d\Omega, \tag{A.11}$$

$$\boldsymbol{H} = -\int_{\Omega} \frac{k\Delta t}{\mu} \left(1 + \frac{\rho_f k}{n_f \mu \theta \Delta t}\right)^{-1} \left(\boldsymbol{\nabla N}_f\right)^T \boldsymbol{\nabla N}_f \ \mathrm{d}\Omega, \tag{A.12}$$

$$\boldsymbol{H}_d = -\int_{\Gamma_d} k_i \Delta t \boldsymbol{N}_f^T \boldsymbol{N}_f \ \mathrm{d}\Gamma_d, \tag{A.13}$$

$$\boldsymbol{H}_{dd} = \int_{\Gamma_d} k_i \Delta t \boldsymbol{N}_f^T \boldsymbol{N}_{df} \ \mathrm{d}\Gamma_d, \tag{A.14}$$

$$\boldsymbol{H}_{df} = -\int_{\Gamma_d} 2 k_i \Delta t \boldsymbol{N}_{df}^T \boldsymbol{N}_{df} \ \mathrm{d}\Gamma_d. \tag{A.15}$$